Numerical Simulation of Gear Pumps

G. Houzeaux
R. Codina

Publication CIMNE Nº-224, April 2003

Numerical Simulation of Gear Pumps

G. Houzeaux
R. Codina

Publication CIMNE Nº-224, April 2003

International Center for Numerical Methods in Engineering
Gran Capitán s/n, 08034 Barcelona, Spain

Numerical Simulation of Gear Pumps

Guillaume Houzeaux* and Ramon Codina†

International Center for Numerical Methods in Engineering (CIMNE)

Edificio C1, Campus Nord UPC

Jordi Girona 1-3, 08 034 Barcelona (Spain)

Abstract

We present in this paper a complete numerical strategy for the study of two gear pumps. This work includes all the steps to follow from the treatment of the CAD geometry until the analysis of the simulation results. In particular we treat the CAD simplification, the meshing of the geometry, the numercial strategy and, finally, the analysis of simulation results.

Contents

*houzeaux@cimne.upc.es

†ramon.codina@upc.es

1 Summary

The work presented in this report was carried out in the framework of the GROWTH project of the European Union, GDR1-1999-10343, from January 2000 to January 2003, and titled "Enhanced design and manufacturing of mini-hydraulic products (MINIHAP)". This main objective of the simulation tasks developed was the...

Study of hydraulic performance using advanced CFD models. Particular emphasis was put in studying the inlet configuration to minimize cavitation effects leading to maximum pumpability and minimum noise effect.

The report mainly treats numerical aspects and tries to define a possible strategy to simulate the dynamics of oil in gear pumps. In particular, we propose to investigate two rotary pumps of fixed displacement type, belonging to the family of gear pumps [1]. They are an external gear pump (also referred to as spur tooth pump) and an internal gear pump (of gerotor type). The study carried out for the analysis of these pumps can be, as in a classical CFD simulation, divided into three main steps, namely the pre-process, the process and the post-process.

The **pre-process** is the generation of the computational domain and its meshing. Unfortunately for the numerical analysts, this is in current CFD problems the most demanding step! When approaching a new fluid dynamics problem, the first task is to understand the physical phenomena we are faced with. In the present case we have to determine the state of the flow (laminar/turbulent), the degree of compressibility of the fluid (incompressible/compressible), etc. The second task consists in making some geometrical approximations in order to reduce the size of the problem without affecting seriously the physics to be solved. For example, if we want to observe the leakage of oil between the casing and the gears, we have to account for the flow in the gap. If this is not the case and the leakage can be assumed negligible, then we can consider separately the inport and outport of the pump. These are important decisions that may change the whole simulation process. Figure 1 illustrates this example. Taking into

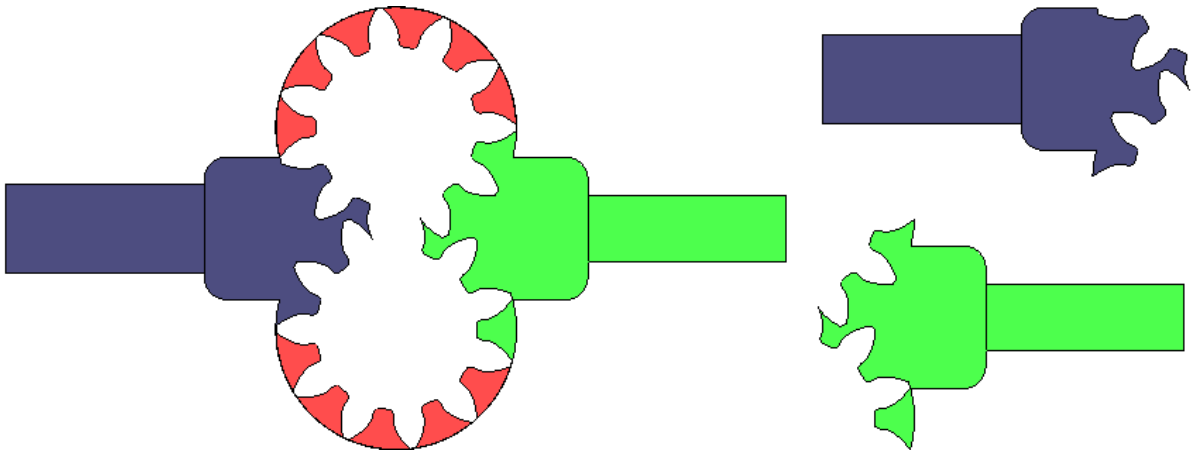

Figure 1: External gear pump. Two dimensional section. (Left) Gap between gears and casing is considered: suction and discharge chambers are connected . (Right) No gap: suction, discharge chambers and cavities are independent.

account the above considerations, we define the computational domain from the CAD geometry. That is we import points, lines, and if available surfaces and volumes, to define a close domain (surface in 2D, volume in 3D) which contains fluid. This task can require some non-negligible work as CAD geometries usually contain unuseful information (symmetry and section lines, remarks, dimensions, etc). The next step consists in meshing this domain, i.e. to divide it into finite elements. Once again the physics of the problem is of great importance at this stage. For example, if we decide to solve the Navier-Stokes equations, we know that elements have to be concentrated near the walls, where we have to capture the sharp velocity gradients present across the boundary layer.

The second step of the CFD simulation is the **process**. It consists in solving the governing equations of the flow problem, which are in our case the Navier-Stokes or the Stokes equations. Figure 2 shows the streamlines obtained on a 2D section of an external gear pump using the Navier-Stokes and Stokes equations. The Navier-Stokes equations (which include a non-linear inertia term) exhibit a larger recirculation in the discharge chamber.

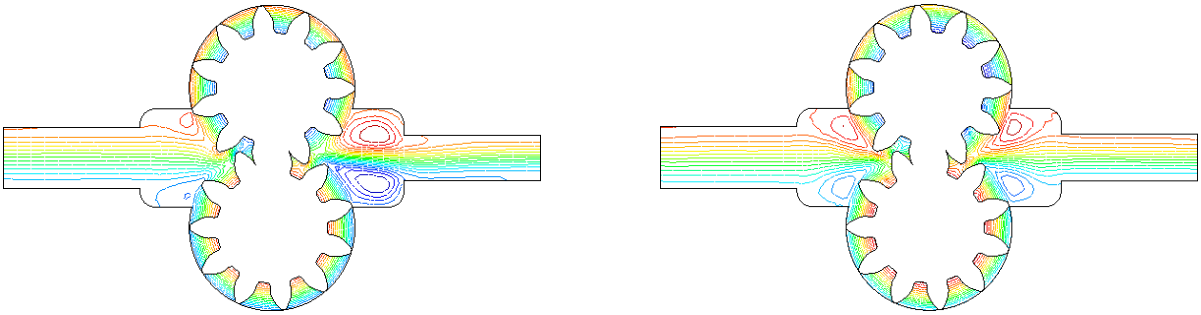

Figure 2: External gear pump. Streamlines. (Top) Navier-Stokes. (Bot.) Stokes.

Finally, the results of the numerical simulation are analyzed in the **post-process** step. According to these results, some modifications on the original geometry can be found necessary, so that we go back to the pre-process step. Figure 3 shows an example of post-process, the streamlines obtained with the simulation of an internal gear pump, which represent some particle paths inside the pump.

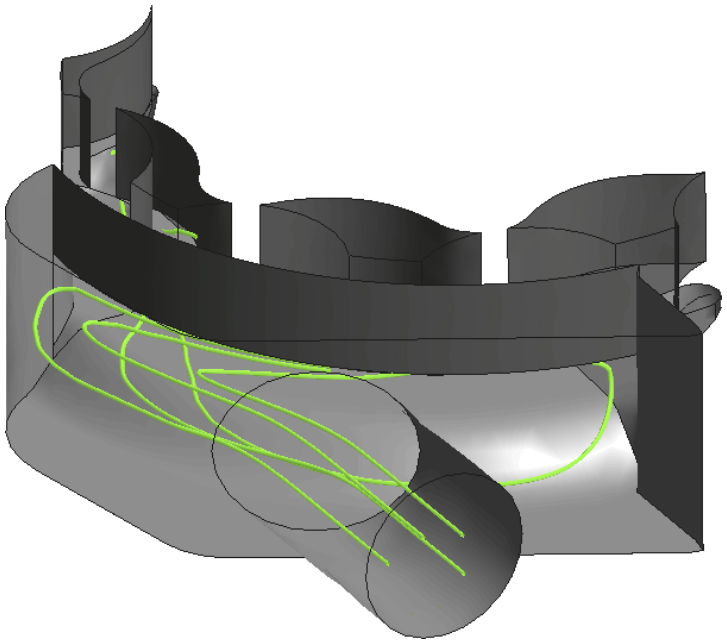

Figure 3: Internal gear pump. Streamlines.

The report is organized as follows. We first introduce the governing equations of the fluid dynamics problem we are faced with, that is the Navier-Stokes equations. Next we present the general numerical strategy to solve these equations, including the weak formulation of the problem as well as the finite element method. Then we present the numerical study of two examples: an external gear pump and an internal gear pump. The external gear pump is studied in much more details because many comments which apply to it also apply to the second test case.

2 Numerical strategy

2.1 Problem statement: incompressible flow equations

2.1.1 The Navier-Stokes equations

We give the expression of the Navier-Stokes equations expressed in a non inertial frame of reference [2]. We denote $\boldsymbol{\omega}$ as the angular velocity of the frame of reference, which we assume constant. Let $\boldsymbol{x}$ be the position vector of a fluid point and Ω be an open bounded domain of $\mathbb{R}^2$ or $\mathbb{R}^3$. Consider the time interval $(0,T)$. The transient Navier-Stokes equations for the velocity $\boldsymbol{u}$ and the pressure p are:

$$\begin{aligned} \rho\partial_t\boldsymbol{u} + \rho(\boldsymbol{u}\cdot\nabla)\boldsymbol{u} + 2\rho\boldsymbol{\omega}\times\boldsymbol{u} - 2\mu\nabla\cdot\boldsymbol{\varepsilon}(\boldsymbol{u}) + \nabla p &= \boldsymbol{f} \qquad \text{in } \Omega\times(0,T), \\ \nabla\cdot\boldsymbol{u} &= 0 \qquad \text{in } \Omega\times(0,T), \end{aligned}$$

where $\boldsymbol{f}$ is the vector of body forces including the the non-inertial term

$$\boldsymbol{f} = -\rho\boldsymbol{\omega}\times(\boldsymbol{\omega}\times\boldsymbol{x}),$$

and $\boldsymbol{\varepsilon}(\boldsymbol{u})$ is the rate of deformation tensor given by

$$\boldsymbol{\varepsilon}(\boldsymbol{u}) = \frac{1}{2}(\nabla\boldsymbol{u} + \nabla\boldsymbol{u}^t).$$

Note that using the continuity equation we have that

$$2\nabla\cdot\boldsymbol{\varepsilon}(\boldsymbol{u}) = \Delta\boldsymbol{u}.$$

The Navier-Stokes equations describe the motion of an incompressible fluid, i.e. a fluid for which the density does not change significantly with the pressure gradients in play. We expect the effects of compression to become important when the velocity of the fluid approach the sound velocity, i.e. the velocity of propagation of the pressure waves. In addition, we assume that the density is constant over the computational domain and is insensitive to pressure variations. The viscosity μ is a measure of the internal friction of the fluid and consequently depends on the temperature of the fluid. Its mechanical role is to eliminate any local deformation. The value of the viscosity for a specific fluid (gas or liquid) is usually measured experimentally as there do not exist suitable theoretical arguments to derive an expression for general fluids. The expression for the viscous term was first considered by Newton who recognized that in a parallel two dimensional flow, the shear stress should be proportional to the rate of deformation. The interpretation of the velocity $\boldsymbol{u}$ in an Eulerian context is simply the velocity of the fluid point measured at a given position and at a given time. The variable p is the mechanical pressure.

The Navier-Stokes equations must be supplied with boundary and intitial conditions. We consider here the following two conditions of Dirichlet and Neumann types:

$$\begin{aligned} \boldsymbol{u} &= \boldsymbol{u}_g \qquad \text{on } \Gamma_D\times(0,T), \\ \boldsymbol{\sigma}\cdot\boldsymbol{n} &= \boldsymbol{t}_n \qquad \text{on } \Gamma_N\times(0,T), \end{aligned}$$

where $\partial\Omega = \Gamma_N\cup\Gamma_D$, $\boldsymbol{n}$ is the outward unit normal to $\partial\Omega$, and $\boldsymbol{\sigma}$ is the stress tensor given by

$$\boldsymbol{\sigma} = -p\boldsymbol{I} + 2\mu\boldsymbol{\varepsilon}(\boldsymbol{u}), \tag{1}$$

$\boldsymbol{I}$ being the n_{d}-dimensional identity. We have chosen as Neumann condition the prescription of the traction $\boldsymbol{\sigma}\cdot\boldsymbol{n}$ because it usually enters naturally the variational form of the problem. Note that a mixed type of boundary prescriptions can also be considered. For example, in the numerical simulation of turbulent flows, it is common to consider an impermeable wall condition ($\boldsymbol{u}\cdot\boldsymbol{n} = 0$) together with the prescription of the tangential components of the traction to emulate the frictional effects of turbulent boundary layers [3].

2.1.2 Dimensionless form

To introduce some magnitude considerations upon the variables of the system we need to non-dimensionalize the equations of motion. If U and L are some characteristic velocity and length respectively we can redefine some dimensionless variables noted with a '*' sign:

$$\boldsymbol{u} \to U \times \boldsymbol{u}^* \ , \ \ x_i \to L \times x_i^* \ , \ \ t \to \frac{L}{U} \times t^* \ , \ \ p \to \rho U^2 \times p^*.$$

Rewritting the momentum and continuity equations in a dimensionless form we get:

$$\begin{aligned} \partial_t \boldsymbol{u}^* + (\boldsymbol{u}^* \cdot \nabla)\boldsymbol{u}^* - \frac{1}{\mathrm{Re}} \Delta \boldsymbol{u}^* + \nabla p^* &= \boldsymbol{f}^* \qquad \text{in } \Omega \times (0,T), \\ \nabla \cdot \boldsymbol{u}^* &= 0 \qquad \text{in } \Omega \times (0,T), \end{aligned}$$

where Re is the Reynolds number defined as:

$$\mathrm{Re} = \frac{\rho U L}{\mu} = \frac{UL}{\nu},$$

with ν being the kinematic viscosity such that $\nu = \mu/\rho$.

2.2 Numerical approximation

2.2.1 Variational formulation

For the sake of clarity we drop the * sign and consider the stationary case. Before going on to the variational formulation, we introduce the linearized Navier-Stokes operator $\boldsymbol{L}$ such that

$$\boldsymbol{L}(\boldsymbol{u}, p) := \begin{bmatrix} \rho(\overline{\boldsymbol{u}} \cdot \nabla)\boldsymbol{u} + 2\rho\boldsymbol{\omega} \times \boldsymbol{u} - 2\mu \nabla \cdot \boldsymbol{\varepsilon}(\boldsymbol{u}) + \nabla p \\ \nabla \cdot \boldsymbol{u} \end{bmatrix},$$

with $\overline{\boldsymbol{u}} = \boldsymbol{u}$ in the nonlinear problem.

We now derive the variational formulation of our problem. Let us introduce the following functional spaces:

$$\begin{aligned} V &= \{\boldsymbol{v} \in H^1(\Omega)^{n_\mathrm{d}} \,|\, \boldsymbol{v}_{|\Gamma_D} = \boldsymbol{0}\}, \\ Q &= L^2(\Omega), \\ U &= \{\boldsymbol{v} \in H^1(\Omega)^{n_\mathrm{d}} \,|\, \boldsymbol{v}_{|\Gamma_D} = \boldsymbol{u}_g\}, \\ P &= \{p \in L^2(\Omega) \,|\, \int_\Omega p \, d\Omega = 0 \text{ if } \Gamma_N = \emptyset\}. \end{aligned}$$

The first step to solve the Navier-Stokes equations is to linearize them. Let us denote denote by m the iteration number of the iterative scheme. For the sake of clarity, we only consider here the Picard linearization, that is,

$$[(\boldsymbol{u} \cdot \nabla)\boldsymbol{u}]^{m+1} \approx (\boldsymbol{u}^m \cdot \nabla)\boldsymbol{u}^{m+1}.$$

We are going to consider two weak forms of the Navier-Stokes equations. The first one is obtained by integrating by parts only the viscous term and is referred to as 0-weak formulation. The second one is obtained integrating by parts the viscous term and half of the convective term and is referred to as 1/2-weak formulation. We define a constant $\flat$ which can take the following values:

$$\begin{aligned} &\text{0-weak formulation:} \quad \flat = 0, \\ &\text{1/2-weak formulation:} \ \flat = 1/2. \end{aligned}$$

The variational formulation of the problem reads as follows. Given $\boldsymbol{u}^0 \in U$, for $m = 0, 1, \ldots$ until convergence, find $(\boldsymbol{u}^{m+1}, p^{m+1}) \in U \times P$ such that

$$a^m(\boldsymbol{u}^{m+1}, \boldsymbol{v}) - b(p^{m+1}, \boldsymbol{v}) + b(q, \boldsymbol{u}^{m+1}) = l(\boldsymbol{v}),$$

for all $(\boldsymbol{v} \times q) \in V \times Q$, where

$$\begin{aligned}
a^m(\boldsymbol{u}, \boldsymbol{v}) &= 2\int_\Omega \mu\boldsymbol{\varepsilon}(\boldsymbol{u}) : \boldsymbol{\varepsilon}(\boldsymbol{v})\, d\Omega + 2\rho\int_\Omega (\boldsymbol{\omega} \times \boldsymbol{u}) \cdot \boldsymbol{v}\, d\Omega \\
&\quad + (1-\flat)\rho\int_\Omega [(\boldsymbol{u}^m \cdot \nabla)\boldsymbol{u}] \cdot \boldsymbol{v}\, d\Omega - \flat\rho\int_\Omega [(\boldsymbol{u}^m \cdot \nabla)\boldsymbol{v}] \cdot \boldsymbol{u}\, d\Omega \\
&\quad + \flat\rho\int_{\Gamma_N} (\boldsymbol{u}^m \cdot \boldsymbol{n})\boldsymbol{u} \cdot \boldsymbol{v}\, d\Gamma, \\
b(p, \boldsymbol{v}) &= \int_\Omega p\nabla \cdot \boldsymbol{v}\, d\Omega, \\
l(\boldsymbol{v}) &= \int_\Omega \boldsymbol{f} \cdot \boldsymbol{v}\, d\Omega + \int_{\Gamma_N} \boldsymbol{t}_n \cdot \boldsymbol{v}\, d\Gamma.
\end{aligned}$$

In this work we use the form given by $\flat = 0$.

2.2.2 Discretization in time and space

We now consider the transient Navier-Stokes equations, together with initial and boundary conditions:

$$\begin{aligned}
\rho\partial_t\boldsymbol{u} + \rho(\boldsymbol{u} \cdot \nabla)\boldsymbol{u} + 2\rho\boldsymbol{\omega} \times \boldsymbol{u} - 2\mu\nabla \cdot \boldsymbol{\varepsilon}(\boldsymbol{u}) + \nabla p &= \boldsymbol{f} && \text{in } \Omega \times (0, T), \\
\nabla \cdot \boldsymbol{u} &= 0 && \text{in } \Omega \times (0, T), \\
\boldsymbol{u} &= \boldsymbol{u}_g && \text{on } \Gamma_D \times (0, T), \\
\boldsymbol{\sigma} \cdot \boldsymbol{n} &= \boldsymbol{t}_n && \text{on } \Gamma_N \times (0, T), \\
\boldsymbol{u} &= \boldsymbol{u}^0 && \text{on } \Omega \times \{0\},
\end{aligned}$$

where the force term and the boundary conditions can depend on time. The time interval where the problem is to be solved is $(0, T)$. The temporal derivative of the velocity has been denoted by $\partial_t\boldsymbol{u}$, t being the time variable.

The time discretization is carried out using the generalized trapezoidal rule, i.e. a finite difference scheme. Let us introduce a uniform partition of the time interval $[0, T]$ and define, for $\theta \in (0, 1]$,

$$\boldsymbol{u}^{n+\theta} := \theta\boldsymbol{u}^{n+1} + (1-\theta)\boldsymbol{u}^n, \quad \delta t := t^n - t^{n-1}, \quad \delta_t\boldsymbol{u}^{n+\theta} := \frac{\boldsymbol{u}^{n+\theta} - \boldsymbol{u}^n}{\theta\delta t},$$

where δt is the time step size and superscript n denotes the approximated solution at time $n\delta t$. According to this integration rule, the time-discretized Navier-Stokes equations are solved as follows. Given an initial condition $\boldsymbol{u}^0$, find $\boldsymbol{u}^{n+1}$ and p^{n+1} for each $n \geq 0$ such that

$$\begin{aligned}
\rho\delta_t\boldsymbol{u}^{n+\theta} + \rho(\boldsymbol{u}^{n+\theta} \cdot \nabla)\boldsymbol{u}^{n+\theta} + 2\rho\boldsymbol{\omega} \times \boldsymbol{u}^{n+\theta} - 2\mu\nabla \cdot \boldsymbol{\varepsilon}(\boldsymbol{u}^{n+\theta}) + \nabla p^{n+\theta} &= \boldsymbol{f}, \\
\nabla \cdot \boldsymbol{u}^{n+\theta} &= 0,
\end{aligned}$$

in Ω, with the following boundary conditions

$$\begin{aligned}
\boldsymbol{u}^{n+\theta} &= \boldsymbol{u}_g && \text{on } \Gamma_D \text{ at time } t^n + \theta\delta t, \\
\boldsymbol{\sigma}^{n+\theta} \cdot \boldsymbol{n} &= \boldsymbol{t}_n && \text{on } \Gamma_N \text{ at time } t^n + \theta\delta t,
\end{aligned}$$

where $\boldsymbol{\sigma}^{n+\theta} = -p^{n+\theta}\boldsymbol{I} + 2\nu\boldsymbol{\varepsilon}(\boldsymbol{u}^{n+\theta})$. The unknown at time step $n+1$ is obtained using the fact that $x^{n+1} = x^n + (x^{n+\theta} - x^n)/\theta$ for each unknown x of the problem. The choice $\theta = 1$ corresponds to the backward Euler scheme, unconditionally stable and of first order. The choice $\theta = 0.5$ corresponds to the Crank-Nicolson scheme, also unconditionally stable but of second order.

Let us consider now the space discretization. Let $\{\Omega^e\}$ be a regular partition of the domain Ω, with index e ranging from 1 to the number of elements n_{e}. The finite element approximation we will consider is conforming, that is, the discrete spaces of test functions and of trial solutions will be linear subspaces of the corresponding spaces for the continuous problem, associated to the partition $\{\Omega^e\}$. We will denote them by a superscript h.

We denote by $x^{n+\theta,m+1}$ the variable x considered at linearization step $m+1$ and time level $n+\theta$. The Galerkin formulation of the problem reads as follows. Given $\boldsymbol{u}_h^{n+\theta,0} = \boldsymbol{u}_h^n \in U_h$, for each time step $n \geq 0$, find for $m = 0, 1, \ldots$ until convergence, $(\boldsymbol{u}_h^{n+\theta,m+1}, p_h^{n+\theta,m+1}) \in U_h \times P_h$ such that

$$\rho(\delta_t \boldsymbol{u}_h^{n+\theta,m+1}, \boldsymbol{v}_h) + a^{n+\theta,m}(\boldsymbol{u}_h^{n+\theta,m+1}, \boldsymbol{v}_h) - b(p_h^{n+\theta,m+1}, \boldsymbol{v}_h) + b(q_h, \boldsymbol{u}_h^{n+\theta,m+1}) = l(\boldsymbol{v}_h), \tag{2}$$

for all $(\boldsymbol{v}_h \times q_h) \in V_h \times Q_h$, where the superscript $n+\theta$ in l denotes that the external forces are evaluated at this time level, whereas the superscript $n+\theta, m$ in the bilinear form a indicates that it is computed with the advection velocity $\boldsymbol{u}_h^{n+\theta,m}$.

It is well-known that the Galerkin formulation can lack stability for three major reasons. The first reason is related to the compatibility of the finite element spaces for the velocity and the pressure which have to satisfy the so-called Ladyzhenskaya-Brezzi-Babuška condition [4]. This condition is necessary to obtain a stability estimate for the pressure; without requiring this condition, the pressure would be out of control. The second reason is attributed to the relative importance of the viscous and convective effects. Finally, the third one appears when the Coriolis force becomes important with respect to viscous effects. We will now present a stabilized formulation, based on the algebraic variational subgrid scale (SGS) model first introduced in [5]. The variational SGS model uses as a starting argument that the lack of resolution achieved by the mesh is responsible for the numerical instabilities. Therefore, the model calculates in some approximate way the unresolved scales of the flow, i.e. the scales smaller than the mesh size. The method is extensively described in [6] and [7].

After time discretization and linearization, the problem can be re-written in a compact form as

$$\rho[\delta_t \boldsymbol{u}^{n+\theta,m+1}, 0]^t + \boldsymbol{L}^{n+\theta,m}(\boldsymbol{u}^{n+\theta,m+1}, p^{n+\theta,m+1}) = \boldsymbol{F} \qquad \text{in } \Omega,$$

where $\boldsymbol{L}^{n+\theta,m}$ is defined as

$$\boldsymbol{L}^{n+\theta,m}(\boldsymbol{u}, p) := \begin{bmatrix} \rho(\boldsymbol{u}^{n+\theta,m} \cdot \nabla)\boldsymbol{u} + 2\rho\boldsymbol{\omega} \times \boldsymbol{u} - 2\mu\nabla\cdot\boldsymbol{\varepsilon}(\boldsymbol{u}) + \nabla p \\ \nabla \cdot \boldsymbol{u} \end{bmatrix},$$

and the force term is defined as

$$\boldsymbol{F} := \begin{bmatrix} \boldsymbol{f} \\ 0 \end{bmatrix}.$$

We finally define the residual of the Navier-Stokes equations $\boldsymbol{R}^{n+\theta,m+1}$ at iteration $m+1$ of the time step $n+\theta$ as

$$\boldsymbol{R}^{n+\theta,m+1}(\boldsymbol{u}_h^{n+\theta,m+1}, p_h^{n+\theta,m+1}) := \rho[\delta_t \boldsymbol{u}_h^{n+\theta,m+1}, 0]^t + \boldsymbol{L}^{n+\theta,m}(\boldsymbol{u}_h^{n+\theta,m+1}, p_h^{n+\theta,m+1}) - \boldsymbol{F}.$$

The viscous term in the right-hand-side can be evaluated in the interior of the elements. The stabilized weak form reads: given $\boldsymbol{u}_h^{n+1,0} = \boldsymbol{u}_h^n \in U_h$, for each time step $n \geq 0$, find for $m = 0, 1, \ldots$ until

convergence, $(\boldsymbol{u}_h^{n+1,m+1}, p_h^{n+1,m+1}) \in U_h \times P_h$ such that

$$\rho(\delta_t \boldsymbol{u}_h^{n+\theta,m+1}, \boldsymbol{v}_h) + a^{n+\theta,m}(\boldsymbol{u}_h^{n+\theta,m+1}, \boldsymbol{v}_h) - b(p_h^{n+\theta,m+1}, \boldsymbol{v}_h) + b(q_h, \boldsymbol{u}_h^{n+\theta,m+1})$$
$$-\sum_{e=1}^{n_e} \int_{\Omega_e} \boldsymbol{L}^{*n+\theta,m}(\boldsymbol{v}_h, q_h)^t \, \boldsymbol{\tau}_e \, \boldsymbol{R}^{n+\theta,m+1}(\boldsymbol{u}_h^{n+\theta,m+1}, p_h^{n+\theta,m+1}) = l(\boldsymbol{v}_h),$$

$\forall\, (\boldsymbol{v}_h, q_h) \in V_h \times Q_h$, where $\boldsymbol{L}^{*n+\theta}$ is the adjoint of $\boldsymbol{L}^{n+\theta}$, given by

$$\boldsymbol{L}^{*n+\theta,m}(\boldsymbol{v}, q) := \begin{bmatrix} -\rho(\boldsymbol{u}^{n+\theta,m} \cdot \nabla)\boldsymbol{v} - 2\rho\boldsymbol{\omega} \times \boldsymbol{v} - 2\mu\nabla\cdot\boldsymbol{\varepsilon}(\boldsymbol{v}) - \nabla q \\ -\nabla \cdot \boldsymbol{v} \end{bmatrix}.$$

$\boldsymbol{\tau}_e$ is the matrix of stabilization parameters, computed in each element as [6]

$$\begin{aligned} \boldsymbol{\tau}_e &= \mathrm{diag}(\tau_1 \boldsymbol{I}, \tau_2), \qquad \text{where} \\ \tau_1 &= \left(\frac{c_1 \mu}{h_e^2} + \rho \frac{c_2 |\boldsymbol{u}^{n+\theta,m}|}{h_e} + \rho c_3 |\boldsymbol{\omega}| \right)^{-1}, \\ \tau_2 &= c_4 \frac{h_e^2}{\tau_1}. \end{aligned}$$

τ_2 contributes to enforcing the incompressibility of the flow, which is excessively relaxed by the term multiplied by τ_1. The values of the algorithmic constants we use are $c_1 = 4$, $c_2 = 2$, $c_3 = 1$, $c_4 = 1$ and h_e is the characteristic element length. For quadratic elements, h_e is taken as half of the element size.

The Navier-Stokes equations are solved using a Finite Element (FE) model based on a stabilized Galerkin method. In fact, it is well-known that the Galerkin formulation can lack stability for three major reasons. The first reason is related to the compatibility of the finite element spaces for the velocity and the pressure which have to satisfy the so-called Ladyzhenskaya-Brezzi-Babuška (LBB) condition [4]. This condition is necessary to obtain a stability estimate for the pressure; without requiring this condition, the pressure would be out of control. The second reason is attributed to the relative importance of the viscous and convective effects. Finally, the third one appears when the Coriolis force becomes important with respect to viscous effects. The stabilized formulation is based on the algebraic variational subgrid scale (SGS) model first introduced in [5]. The variational SGS model uses as a starting argument that the lack of resolution achieved by the mesh is responsible for the numerical instabilities. Therefore, the model calculates in some approximate way the unresolved scales of the flow, i.e. the scales smaller than the mesh size. The method is extensively described in [6] and [7]. The time discretization is carried out using the generalized trapezoidal rule, i.e. a finite difference scheme.

2.2.3 Some finite elements

In this work we will consider two types of element using both equal order interpolation for the velocity and the pressure. The Q1/Q1 element is continuous and bilinear (trilinear in three dimensions) in both velocity and pressure. We will also work with the P1/P1 element, continuous and linear in velocity and pressure. These elements do not satisfy the LBB condition and therefore require the use of stabilization.

3 External gear pump

3.1 Introduction

Volk [8]: "Simply stated, a pump is a machine used to move liquid through a piping system, and to raise the pressure of the liquid".

The gear pump we consider is sketched in Figure 4. The pump works as follows. The shaft of one of the gears is driven by a motor: this is the driving gear. It engages around the other one, called the driven gear. When the teeth of the two gears start disengaging (near the center of the cavity), the consequent

low pressure sucks in the fluid. Upon further rotation, the fluid is trapped in the space between this cavity and the casing. The fluid is then carried around towards the outlet side of the pump. As in principle it cannot flow back through the gap between the teeth and the casing and neither through the engaged teeth of the gears, it is entirely ejected to the outlet. Therefore, unlike a centrifugal fan (for example), the flow rate is expected not to depend on the pressure difference between the inlet and outlet. At high pressures however, some fluid may slip along the casing walls from the outlet (high pressure) to the inlet (low pressure). Thus the efficiency of the pump may be affected. For example, it is well known that a a higher viscous fluid, the leakage will be smaller; however, it requires more power to provide the same rotational speed.

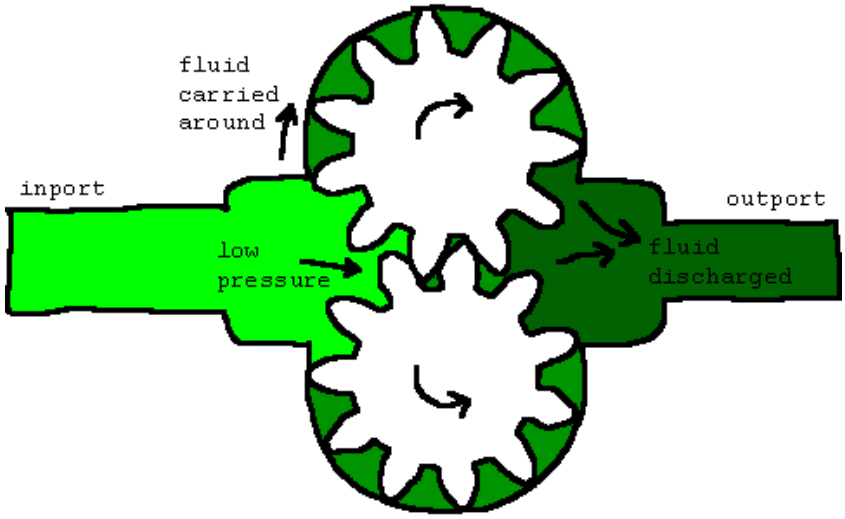

Figure 4: External gear pump. Section at symmetry line.

If we assume that all the fluid trapped between the teeth is delivered to the outport (no leakage), the volume flow rate Q [mm^3/s] furnished by the pump is directly proportional to the velocity of rotation ω [rad/s] of the gears. The constant of proportionally is called the volumetric constant and is referred to as C_v [mm^3/rad]:

$$Q = C_v \omega.$$

The units considered along this work are mm, s and kg.

The gear pumps have many applications. In the car industry, they are used to pump oil towards the elements to be lubricated; in construction equipment they work as an hydraulic power unit (e.g. excavator); they deliver gas in petrol stations, as the volume of fluid delivered by second being directly proportional to the velocity of rotation of the gears; they can serve as a counter (e.g. for metering water consumption) for they are reversible and can therefore be engaged by the flow of fluid; they are used as hydraulic pumps in snow plows, etc.

As a first approach we study a section of the real pump. In particular, we want to be able to estimate the pressure distribution in the suction side to avoid cavitation. In fact, hydraulic oils contain around 10% of dissolved air. If the pressure at the inlet is to low (in our case the atmospheric pressure), the depression needed to suck in the fluid is propitious to the onset of cavitation. Cavitation affects the pumping capability of the pump as the gear cavities are not filled completely with oil. Actually the scenario is worse, as once cavitation has occurred, a subsequent increase of pressure provokes the collapses of the vapor bubbles. The resulting compression waves contribute to the erosion of tshe structure and the generation of high level noise.

The study of cavitation is not addressed in this study. But the numerical simulations will allow us to detect the zones where the pressure is more likely to fall below the vapor pressure of the fluid. This study will help therefore to orient the modification to carry out on the original geometry to improve the

efficiency of the pump.

The study of this pump is organized as follows. We first explain how to prepare the geometry obtained on a CAD program for a simulation experiment. In particular, we discuss the possible geometrical modifications which enable to simplify the study of the problem without affecting the desired order of accuracy of the results. We then give the physical properties of the fluid and physical aspects of the flow. In the next section we give some numerical results. They include steady as well as transient simulations using the Stokes and Navier-Stokes equations in two dimensions, and also transient Stokes simulations in three dimensions.

3.2 Geometry simplification

The CAD geometry of the gear pump is shonw in Figure 5. When importing the geometry from a CAD program, a lot of points are created on the contour lines of the apparatus. The first task is to collapse some of these points to obtain a maximum number of continuous lines. Figure 6 (Left) shows the geometry (before and after collapse) of a tooth.

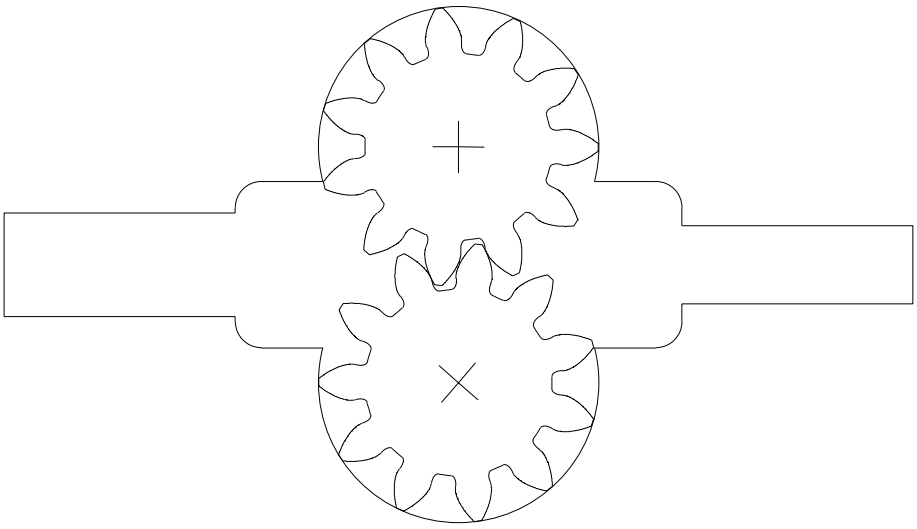

Figure 5: External gear pump. CAD geometry. Initial configuration.

The second task consists in simplifying the bevelled corners of the teeth by moving outward the edge points onto the tip lines. This change is easy but very effective. In fact, on this modified geometry we can generate a structured mesh in the gap between the teeth and the casing. This enables us to control the number of elements we want to use to solve the boundary layer that will appear in the gap.

The first simulations are going to be performed on the complete geometry, in its initial position. Therefore, we have to mesh the entire geometry, except the zone of intersection of the two gears, where we assume that the fluid does not flow. This mesh is composed of 10867 triangular elements and is shown in Figure 7. Note in particular the structured mesh of the gap.

3.3 The meshing

In common CFD applications, the meshing takes a (too) huge part of the total computational process. Some work has been done so that this process be less tedious.

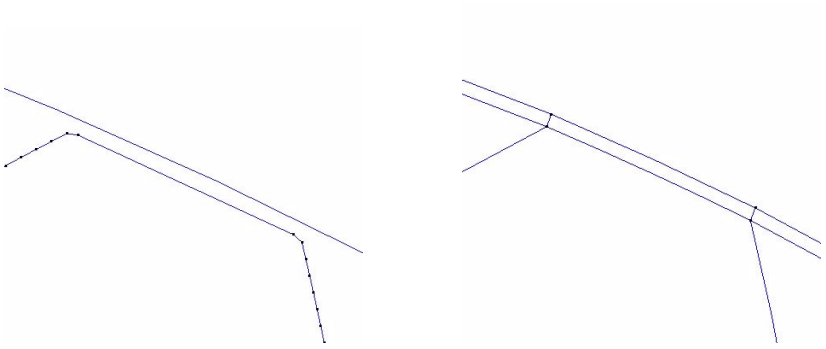

Figure 6: External gear pump. Simplification of the tooth geometry. (Left) Before. (Right) After.

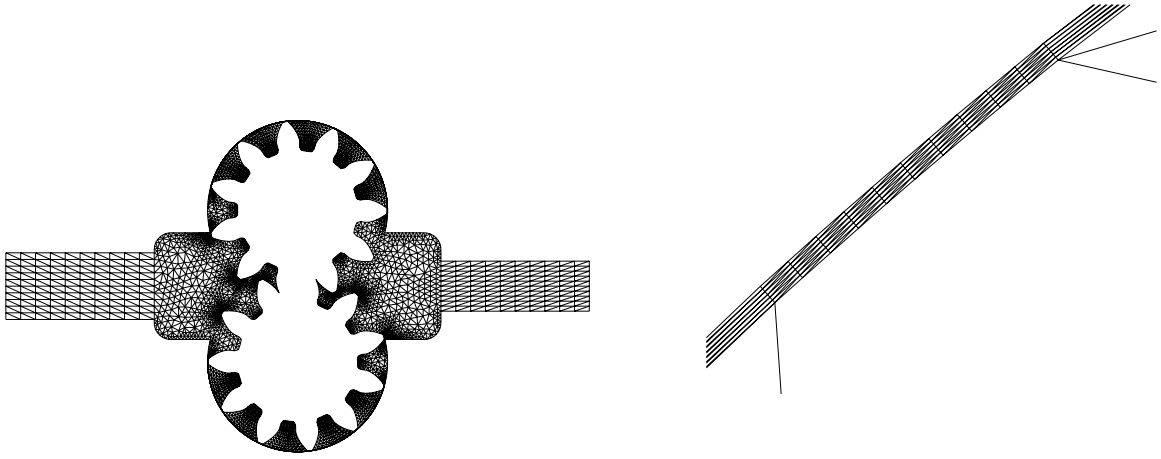

Figure 7: External gear pump. Mesh of the initial geometry. (Left) Whole mesh. (Right) Structured mesh in the gap.

3.3.1 Mixing types of element

In two dimensions, we deel with two types of elements, namely triangles and quadrilaterals. On the one hand, triangles are more suited for complicated geometries as they allow strong skewness which can be prohibitive for quadrilaterals, for example in the engagment zone of the driving and driven teeth. See Figure 8 (Top) (Left) and (Bot.) (Left). On the other hand, quadrilaterals are better adapted for boundary layers flows, for example in the gap between the teeth and the body. Using triangles in this zone would uselessly duplicate the number of elements. In addition, it is well known that triangles are more diffusive than quadrilaterals and therefore we gain precision by using quadrilaterals whenever it is possible. See Figure 8 (Top) (Right) and (Bot.) (Right). In order to be able to deal with both types of elements, the CFD program has been adapted. Note that the final mesh is still conforming as only linear or bilinear interpolation is used all along this work.

3.3.2 3D configuration

Three-dimensional simulations are approached in two manners. The first one consists in considering only the suction side of the pump, which is the zone of major interest. Doing this we do not have to solve the gap between the teeth and the body and therefore avoid meshing this complicated zone. The meshing is therefore straightforward, see for example Section 3.5.5. The other approach consists in assuming that the cross-flow (in the perpendicular direction to the 2D section) is slow, and therefore we

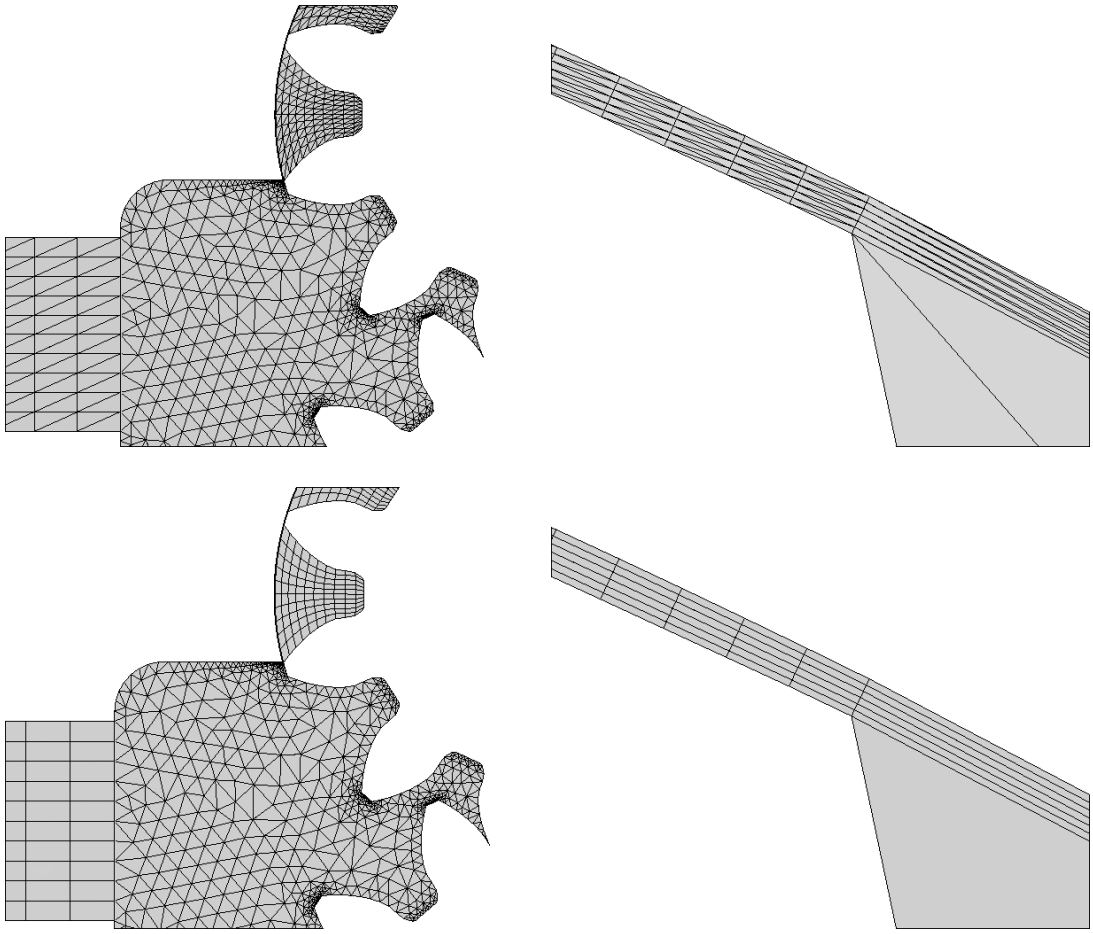

Figure 8: External gear pump. Comparison of different meshings. (Top) Using triangles. (Bot.) Using triangles and quadrilaterals.

avoid needing a fine mesh in this direction. According to this consideration, a simply way of generating a 3D mesh is to extend the mesh of the 2D section in some few layers in the perpendicular direction. This is shown in Figure 9. The suction and discharge chamber can be simulated through a domain decomposition method, as shown in Figure 10.

3.4 Data of the problem

The volumetric constant of the pump C_v is:

$$C_v = 36 \text{ cm}^3/\text{rotation} = 5.73 \text{ cm}^3/\text{rad}.$$

The pump works at 1500 rpm, which corresponds to an angular velocity of

$$\omega = 157.08 \text{ rad/s}.$$

The properties of the oil we are considering are:

$$\mu = 2.98 \times 10^{-5} \text{ kg/mm s},$$
$$\rho = 9.21 \times 10^{-7} \text{ kg/mm}^3.$$

The pump discharges a constant flow rate at constant velocity of rotation but has no control on the global pressure rise. The amount of pressure is controlled by the workload imposed on it. In the

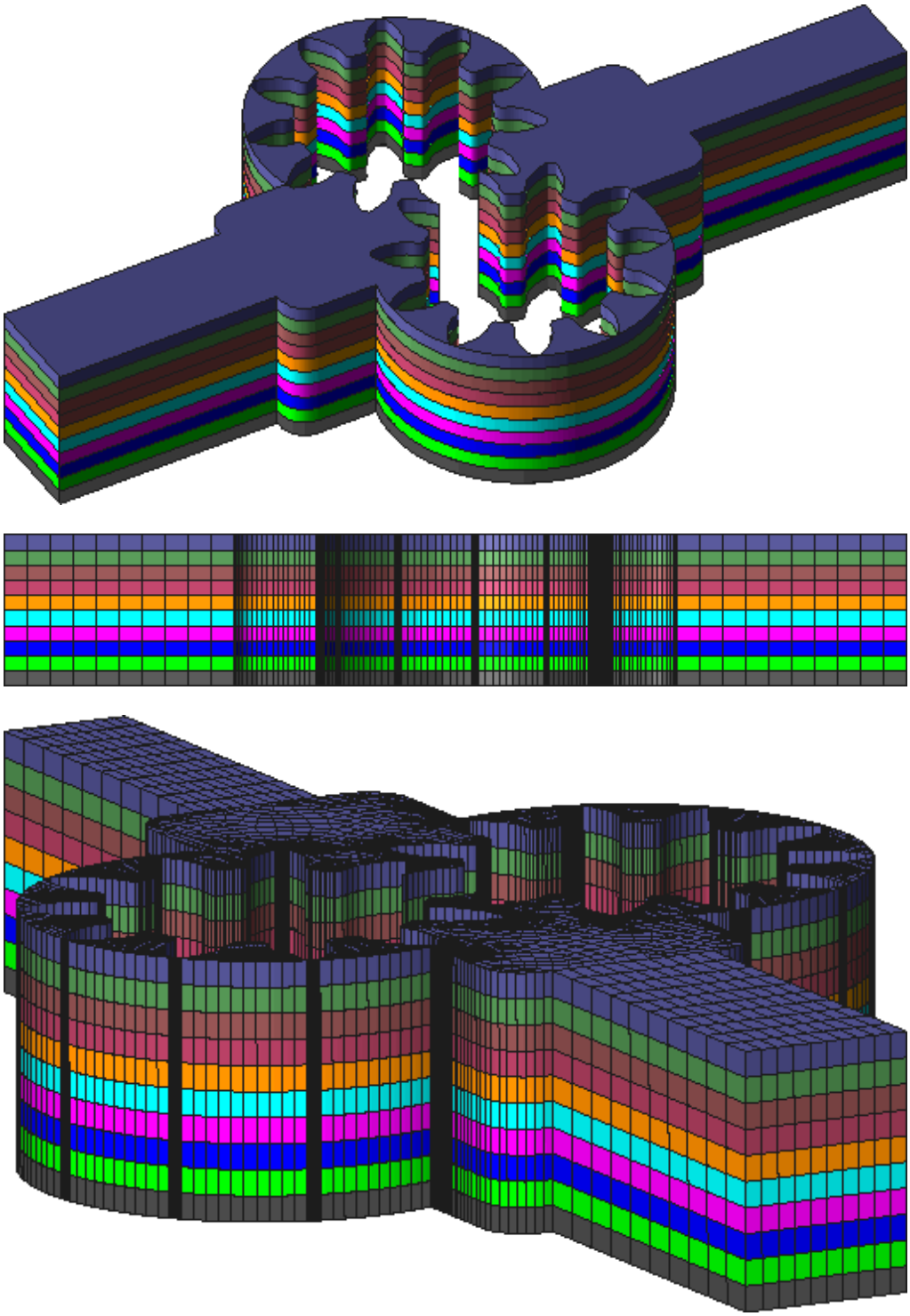

Figure 9: External gear pump. Generation of the 3D mesh from a 2D mesh. (Top) General view of the different layers. (Mid.) Side view of the mesh. (Bot.) Inclined view of the mesh.

experiment, the pressure at the outlet is fixed to a value p_o of 10 bars. At the inlet, the pressure is that of the reservoir, i.e. the atmospheric pressure p_a. We have the following conversions:

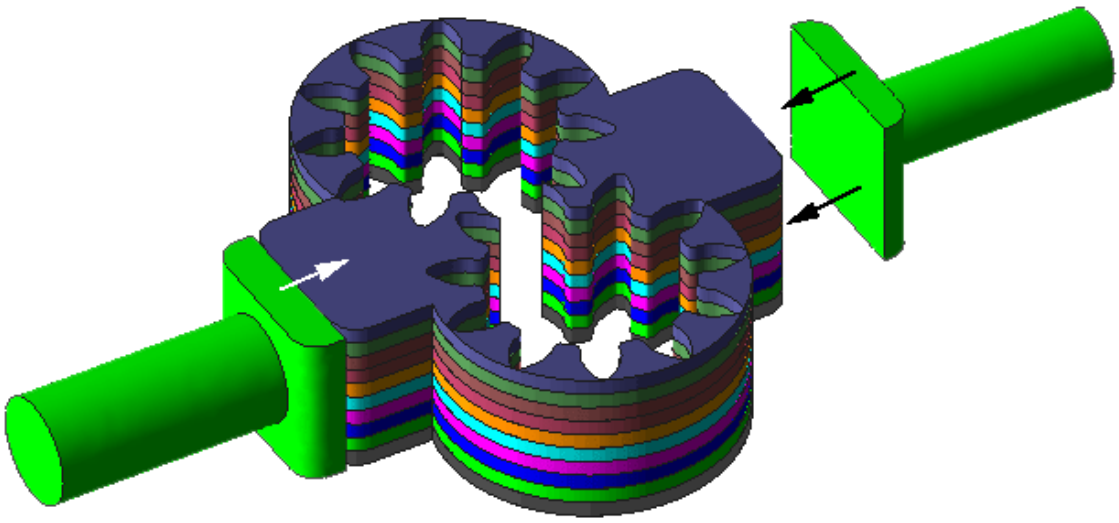

Figure 10: External gear pump. Domain decomposition method to solve the entire 3D model.

$$\begin{aligned} 1 \text{ bar} &= 10^5 \quad \text{Pa}, \\ 1 \text{ Pa} &= 1 \quad \text{N/m}^{\,2}, \\ 1 \text{ N} &= 1 \quad \text{kg/m } s^2. \end{aligned}$$

So the prescription of the pressure in our unit system is obtained using the following formula:

$$p = 10^2 p(\text{in bars}) \, \text{kg/mm s}^2,$$

and we have

$$\begin{aligned} p_a &= 10^2 \, \text{kg/mm s}^2, \\ p_o &= 10^3 \, \text{kg/mm s}^2. \end{aligned}$$

The pressure in prescribed in a weak way, by specifying the traction as

$$\begin{aligned} \boldsymbol{\sigma} \cdot \boldsymbol{n} &= [p_a, 0(,0)]^t \qquad \text{at inport}, \\ \boldsymbol{\sigma} \cdot \boldsymbol{n} &= [-p_o, 0(,0)]^t \qquad \text{at outport}, \end{aligned}$$

where the third component only makes sense in three dimensions. We have assumed that the x-axis is perpendicular to the inport and outport lines (surfaces in 3D). The minus sign before the pressure at the outport is due to the sign of the outward normal. Note that the normal component of the traction is the pressure if and only if the flow is fully developed (see the expression for the stress tensor (1)).

3.5 Results

3.5.1 Steady flow in the whole pump

As a first study, we solve the steady Stokes problem (which is linear) in the whole domain. For the computational domain, we choose the initial configuration of the apparatus, and prescribe on the gears boundaries their own velocity of rotation. We hope we can obtain a pseudo steady state to have a rough idea of the behavior of the fluid. Figure 11 shows the boundary conditions imposed on the computational domain.

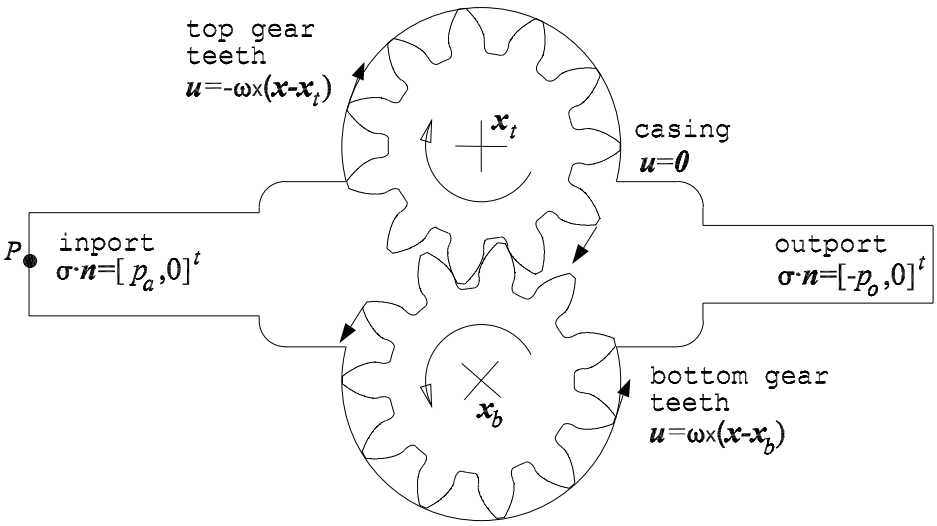

Figure 11: External gear pump. Stationary Stokes solution. Geometry and boundary conditions.

Figure 13 shows the results of the simulation. The (Top) part shows the streamlines. We observe that strong recirculation zones are present in the corners of the casing. The (Mid.) part gives the pressure distribution in the pump. We first observe that the pressure distribution is almost uniform in the space between the teeth and the casing, and that it goes from its inflow value to its outflow in stairways steps along the housing wall. The pressure distribution along this wall is shown in Figure 12, where the reference point P is depicted in Figure 11.

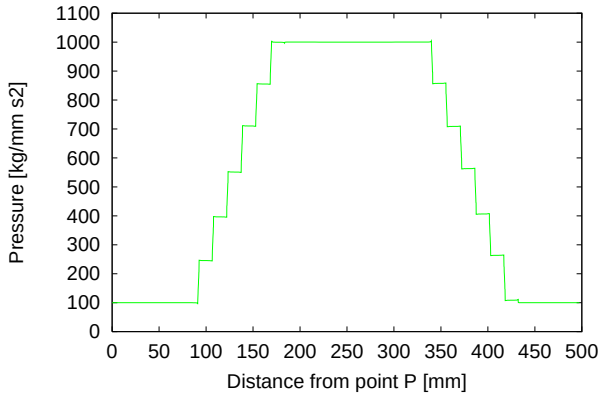

Figure 12: External gear pump. Stationary Stokes solution. Pressure distribution along the casing wall.

The lower pressure is obtained in almost the entire suction zone of the pump and is lightly below the atmospheric pressure, around 92 kg/mm s^2. The lowest pressure is found in the region of separation of the gears, where the fluid is sucked in at high velocity, as shown in Figure 13 (Bot.). Figure 14 (Bot.) shows the velocity vectors and enable to appreciate the zones where the fluid is accelerated. In particular, we note that fluid is ejected to the outport at a high velocity where the gears engage. The maximum velocity attained by the fluid is 14549 mm/s ($\approx$ 54,4 km/h).

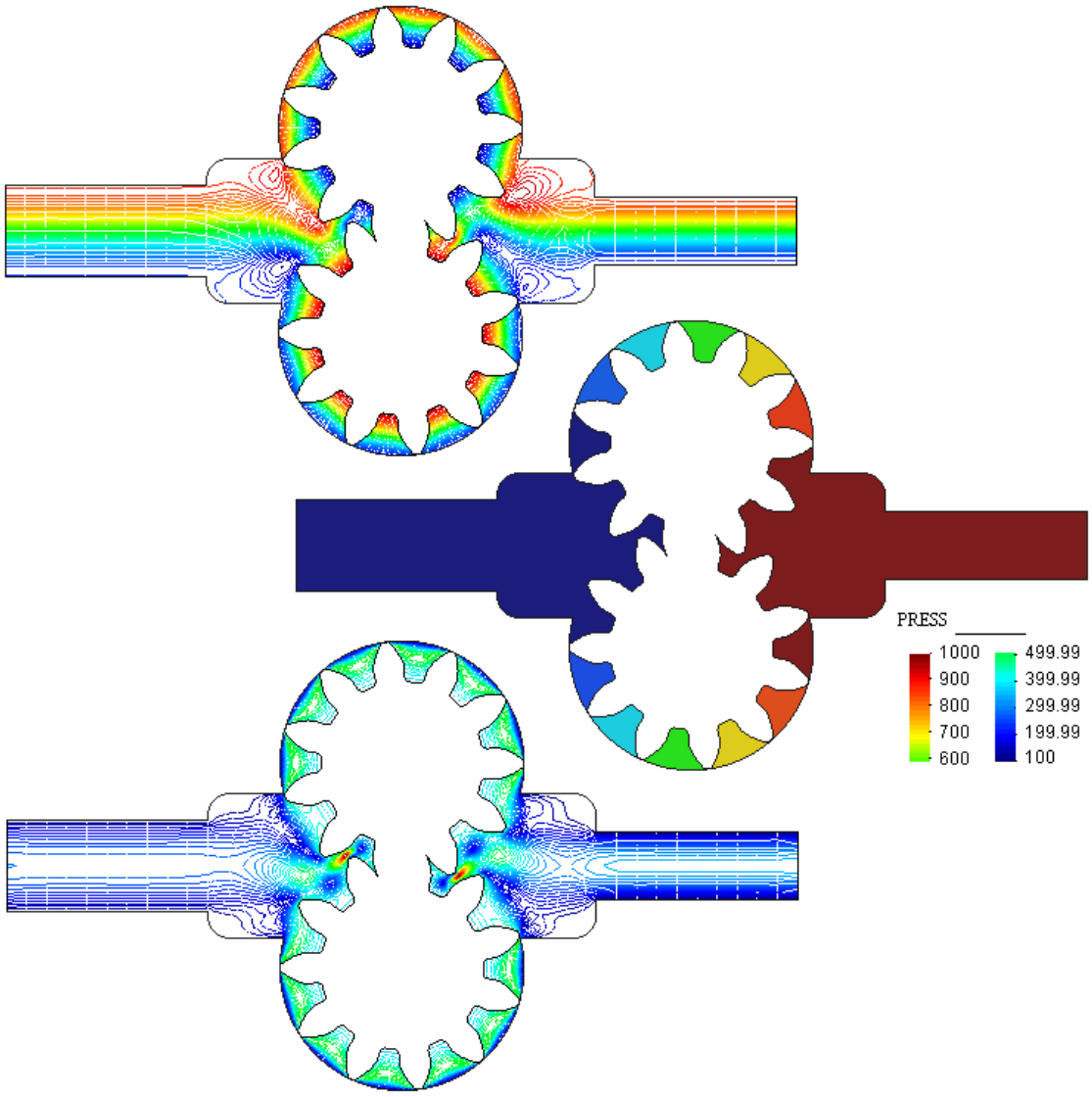

Figure 13: External gear pump. Stationary Stokes solution. (Top) Streamlines. (Mid.) Pressure. (Bot.) Velocity module.

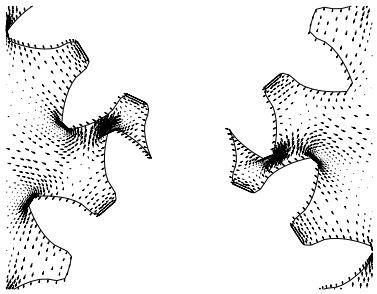

Figure 14: External gear pump. Stationary Stokes solution. Velocity vector near engagement and disengagement zones.

3.5.2 Steady flow between teeth

We now investigate the flow in the cavity formed by two consecutive teeth and the casing. The problem is solved in the rotating frame of reference, of angular velocity $\boldsymbol{\omega} = [0, 0, \omega]^t$, so that the velocity on the casing is prescribed to $-\boldsymbol{\omega} \times \boldsymbol{x}$, with rotation center located at the origin. Three meshes of different levels of refinement have been used. The coarse mesh has 100 Q1/Q1 elements, the medium mesh has 400 Q1/Q1 elements and the finest mesh has 1600 Q1/Q1 elements.

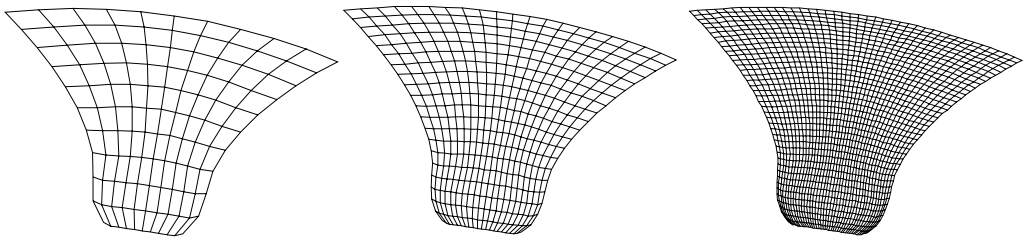

Figure 15: External gear pump. Steady flow between teeth. Coarse, medium and fine meshes.

Figure 16 (Left) shows the pressure distribution along the computational wall. As expected, we observe that the discontinuity in velocity produces high pressure gradients near the corners: therefore, we expect the pick of pressure to be higher and higher as the mesh is refined (for the Stokes flow we would have a singularity at this corners; for the Navier-Stokes flow, these points are not singular but exhibit high pressure gradients). But away from this points, the pressure distribution is quite similar for these three meshes. We also observe that there is no net pressure gradient between inflow and outflow corners. In fact, we already observed in Figure 12 that the pressure varies almost exclusively due to friction in the gap between the teeth and the casing. Figure 16 (Right) gives the velocity distribution along the vertical centerline of the computational domain. We see that even the coarse mesh capture sufficiently well the velocity profile. We conclude that a rather coarse mesh (100 Q1/Q1 elements) is sufficient to obtain reasonable results.

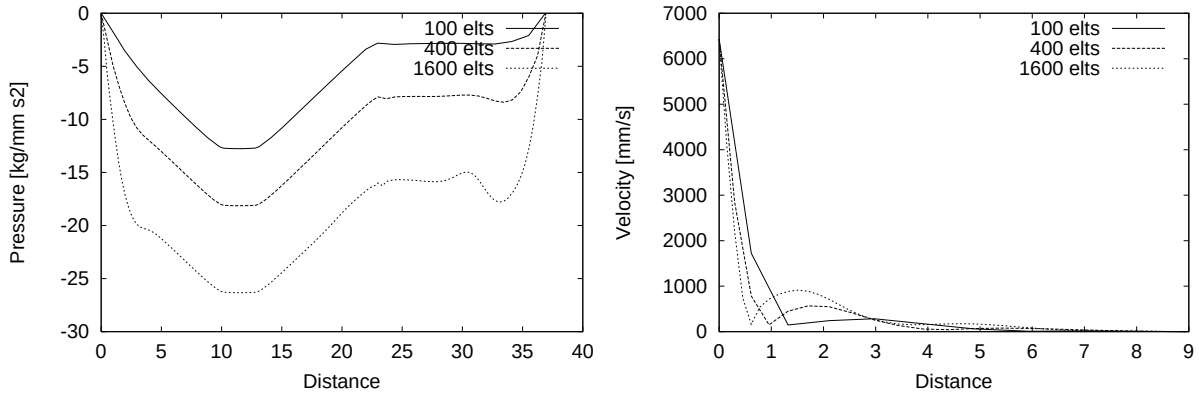

Figure 16: External gear pump. Steady flow between teeth. (Left) Pressure along walls. (Right) Velocity along centerline.

Finally, Figure 17 shows the solution obtained on the finest mesh. We note that inside the cavity the pressure is almost due to the centrifugal force, except at the top right corner where it accommodates the recirculation zone. In fact, we note that for a rotating two-dimensional flow the centrifugal force can be absorbed by the pressure term; we have that

$$\boldsymbol{\omega} \times \boldsymbol{\omega} \times \boldsymbol{x} = -\frac{1}{2}\nabla(|\boldsymbol{\omega} \times \boldsymbol{x}|^2).$$

In addition, we notice that

$$\nabla \times (\boldsymbol{\omega} \times \boldsymbol{u}) = |\boldsymbol{\omega}| \nabla \cdot \boldsymbol{u} = 0,$$

which means that the Coriolis term is the gradient of a function. Therefore, both the centrifugal force and the Coriolis terms can be included in the pressure term. This is possible because the flow is confined; if it were not the case, then we could not impose a physical traction on the Neumann contour. Hence, we expect the solution in velocity to be the same than that of a fixed cavity.

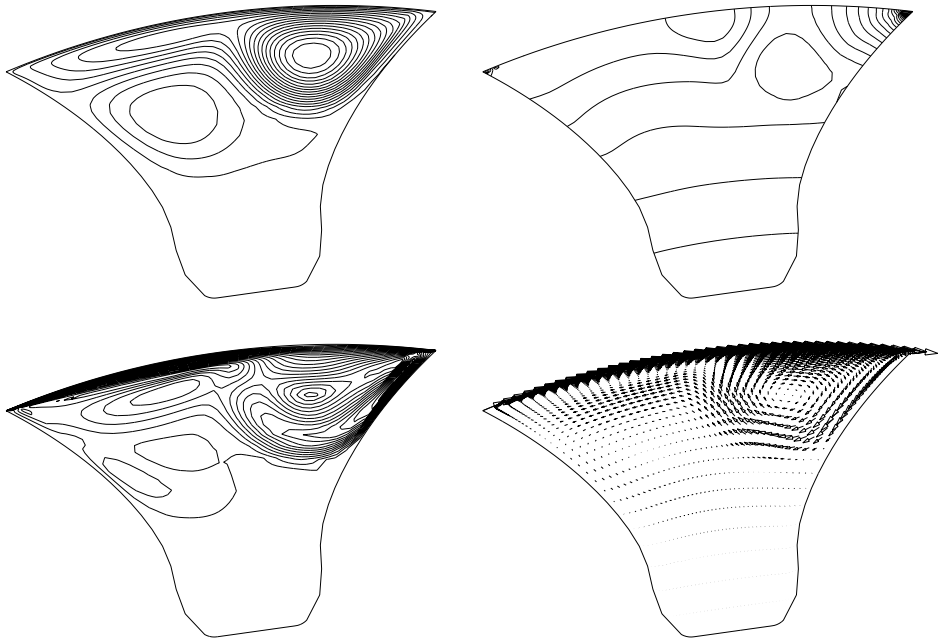

Figure 17: External gear pump. Steady flow between teeth. (Top) (Left) Streamlines. (Top) (Right) Pressure. (Bot.) (Left) Velocity module. (Bot.) (Right) Velocity vectors.

3.5.3 Transient simulation: Stokes problem

The transient case is quite delicate because the contact point of the teeth in the zone of engagement changes at all time. One possible numerical would be to set up an iteration-by-subdomain method to couple three subdomains: one for each gear, and one for the casing. The casing is coupled with both gears outside the zone of intersection of the gears subdomains, while the gears are coupled together. Two types of iteration-by-subdomain method have been test without success, namely the Dirichlet/Robin method [9] and the Robin/Robin method. The idea is sketched in Figure 18

The main difficulty of this example is the treatment of the zones of engagement and disengagement of the teeth. A nice alternative consists in defining a new geometry and a new mesh at each time step of the numerical simulation, the position of the gears being known a priori. Then we solve successively the flow equations on each geometry taking as a previous time step solution the interpolated variables obtained on the previous geometry.

In fact, we can take advantage of the numerical strategy based on an *implicit* solution of the Navier-Stokes (or Stokes) equations for which we can afford relatively large time steps. In addition, by using the backward Euler time integration scheme, which is unconditionally stable for fixed meshes, we can

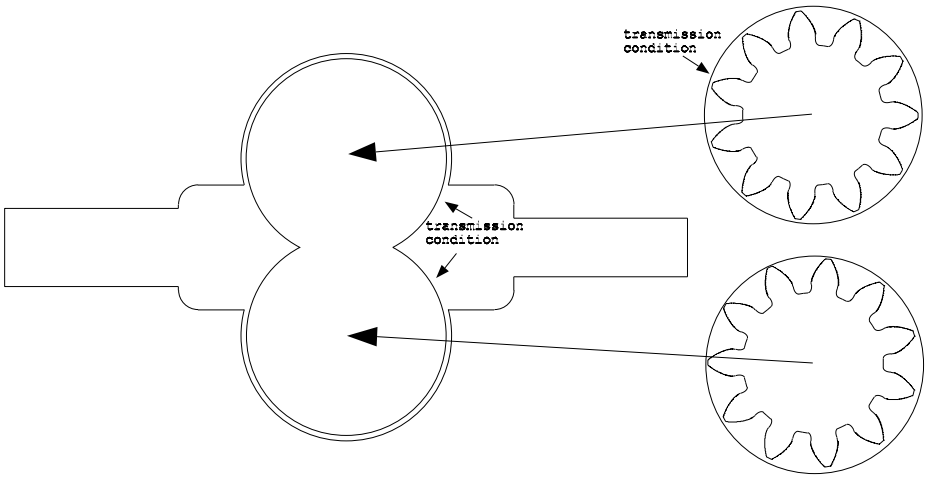

Figure 18: External gear pump. A domain decomposition coupling for the gears and casing.

expect the resulting numerical strategy to be stable. In order to choose the time step we have to make a compromise which as always, faces accuracy with computation time. On the one hand, the time step must be large enough so that we do not have to calculate too many geometries and to generate too many meshes. On the other hand, the time step must be small enough to capture the important time scales of the flow. We assume that the leading period of the flow will be that of a tooth passing and that we can neglect the effect of smaller scales on the mean flow. According to these considerations, we decide to solve 10 times the flow equations between two tooth passings (which is approximately the number of points to solve with sufficient accuracy a sine type signal). Therefore we set:

$$\delta t = \frac{2\pi}{110\omega} \approx 2.63 \times 10^{-4} \text{ s.}$$

Figure 19 shows four geometries calculated for four consecutive time steps, the first figure being the initial configuration.

Figure 20 shows two zooms of the mesh at crucial points: the passing of a gear by a casing corner and the zone of engagement of the two gears. The ten meshes generated are composed by an average of 12230 P1/P1 elements.

We now study the stability of this numerical strategy, which consists in couling different meshes at different time steps. Let us consider the variational form of the Navier-Stokes equations (2) for the backward Euler scheme without force term. For the sake of clarity we drop both the space discretization and linearization indices. For each $n \geq 0$ we have

$$(\boldsymbol{u}^{n+1} - \boldsymbol{u}^n, \boldsymbol{v}) + \delta t a^{n+1}(\boldsymbol{u}^{n+1}, \boldsymbol{v}) - \delta t\, b(p^{n+1}, \boldsymbol{v}) + \delta t\, b(q, \boldsymbol{u}^{n+1}) = 0. \tag{3}$$

We observe that we only need from the previous time step the velocity $\boldsymbol{u}^n$. The numerical strategy is straightforward: at each time step $n+1$ we use the corresponding mesh to solve Equation (3) and interpolate the solution obtained at time step n on the previous mesh on the current mesh to get $\boldsymbol{u}^n$. Let us denote $I^{n+1}(\boldsymbol{u}^n)$ the solution obtained on the mesh used at time step n and interpolated on the mesh used at time step $n+1$.

We noted previously that the backward Euler scheme is unconditionally stable, at least for a fixed mesh. Let us recall how this can be shown. First we take $\boldsymbol{v} = \boldsymbol{u}^{n+1}$ and $q = p^{n+1}$ in Equation (3). We obtain

$$||\boldsymbol{u}^{n+1}||^2_{0,\Omega} - (\boldsymbol{u}^n, \boldsymbol{u}^{n+1}) + \delta t a(\boldsymbol{u}^{n+1}, \boldsymbol{u}^{n+1}) = 0. \tag{4}$$

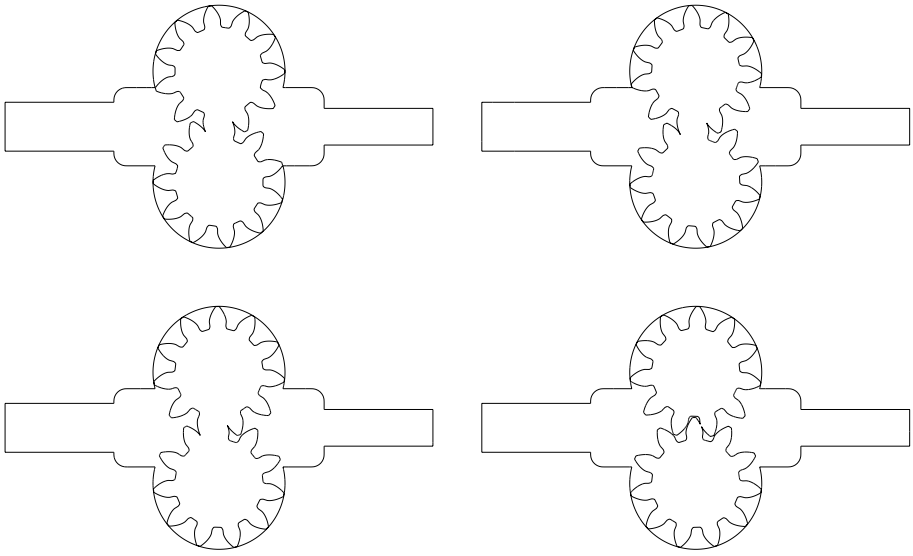

Figure 19: External gear pump. Geometries at different time steps: 0, δt, $2\delta t$, $3\delta t$.

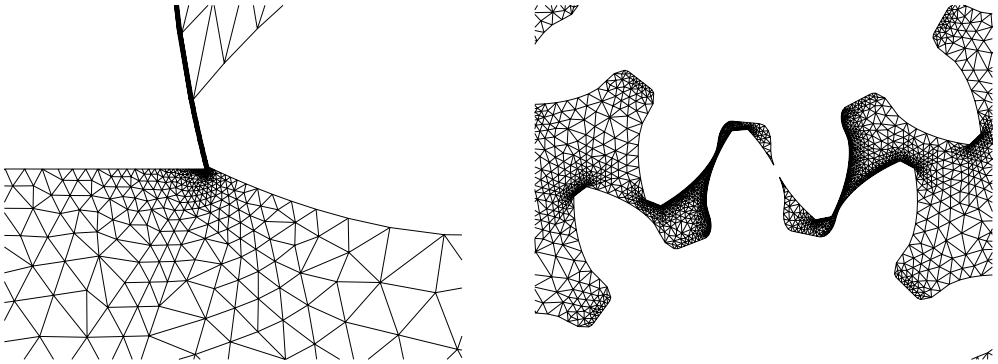

Figure 20: External gear pump. Zooms on meshes. (Left) Time δt, top gear passing near casing corner. (Right) Time $3\delta t$, engagement and disengagement zones.

By noting that

$$(\boldsymbol{u}^n, \boldsymbol{u}^{n+1}) \leq \frac{1}{2}||\boldsymbol{u}^{n+1}||^2_{0,\Omega} + \frac{1}{2}||\boldsymbol{u}^n||^2_{0,\Omega},$$

Equation (4) yields

$$\frac{1}{2}||\boldsymbol{u}^{n+1}||^2_{0,\Omega} - \frac{1}{2}||\boldsymbol{u}^n||^2_{0,\Omega} + \delta t\, a(\boldsymbol{u}^{n+1}, \boldsymbol{u}^{n+1}) \leq 0. \tag{5}$$

Upon summation from $n = 0$ to $n = k$ the latter equation gives

$$||\boldsymbol{u}^{k+1}||^2_{0,\Omega} + 2\delta t \sum_{n=0}^{k} a(\boldsymbol{u}^{n+1}, \boldsymbol{u}^{n+1}) \leq ||\boldsymbol{u}^0||^2_{0,\Omega}.$$

In addition, we have that the bilinear form a is coercive and therefore non-negative, so that the latter equation gives

$$||\boldsymbol{u}^{k+1}||^2_{0,\Omega} \leq ||\boldsymbol{u}^0||^2_{0,\Omega}, \tag{6}$$

which states that the numerical scheme is stable. Now let us see what happens in our case. Remember that the solution of time step n is that interpolated from the previous mesh. Equation (5) must be replaced by:

$$\frac{1}{2}||\boldsymbol{u}^{n+1}||^2_{0,\Omega} - \frac{1}{2}||I^{n+1}(\boldsymbol{u}^n)||^2_{0,\Omega} + \delta t\, a(\boldsymbol{u}^{n+1}, \boldsymbol{u}^{n+1}) \leq 0,$$

so that when summing from $n = 0$ to $n = k$, we cannot cancel any terms and therefore we have no straightforward way to prove the stability estimate given by Equation (6). However, all the numerical experiments carried out here have proven to be stable.

Let us go back to the simulation results. As an initial condition, we solve in the initial configuration the stationary Stokes flow. Then, further time steps are solved using the transient Stokes equations. Figure 21 shows the convergence history of the simulation. The residual is the L_2 residual of the velocity calculated over each nodes of each mesh for two consecutive time steps. The fact that the residual goes to zero means that the velocity is periodic with period $2\pi/(11\omega)$ s $\approx 2.63 \times 10^{-3}$ s. The numerical scheme is stable.

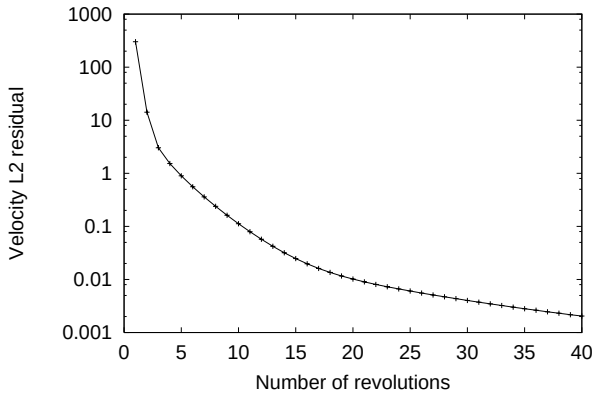

Figure 21: External gear pump. Transient Stokes flow. Convergence history.

Figure 22 shows the velocity and pressure distributions at a point P located on the horizontal centerline of the pump and some short distance before the gear separation. It confirms the periodic behavior of the flow. Figure 23 shows the velocity vectors evolution in the zones of disengagement and engagement of the gears. We observe very high velocities near the intersections. Figure 24 gives the streamline contours for the same time steps. Figure 25 shows some pressure contours in the suction part. Minimum pressure is attained in the small gap between the first disengaging teeth of the top and bottom gears. This very low pressure is responsible for the progressive filling of cavity, and the high velocities in this zone are due to the small gap between the teeth.

As in the case of the steady simulation of the Stokes problem, we observe strong recirculation zones in the corners of the casing. They induce an unnecessary loss of energy, and streamlined profiles may be more appropriate in this part of the pump. In addition, these corners are not desirable for the change of momentum suffered by the fluid to flow around the corner must be accompanied with high pressure gradients.

Let us now analyze the flow through the gap between a tooth and the casing. We consider the azimuthal component of the velocity along a line passing through the gap of length $2H = 0.095\,\text{mm}$. The radius $r_1 = 26.92\,\text{mm}$ of the gear being large and therefore the curvature being small, the flow in

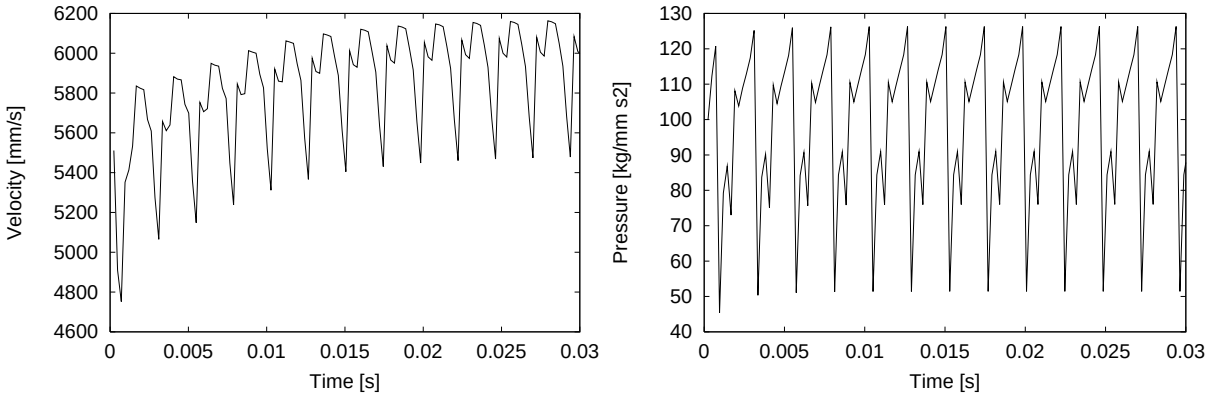

Figure 22: External gear pump. Transient Stokes flow. (Left) Velocity at point P. (Right) Pressure at point P.

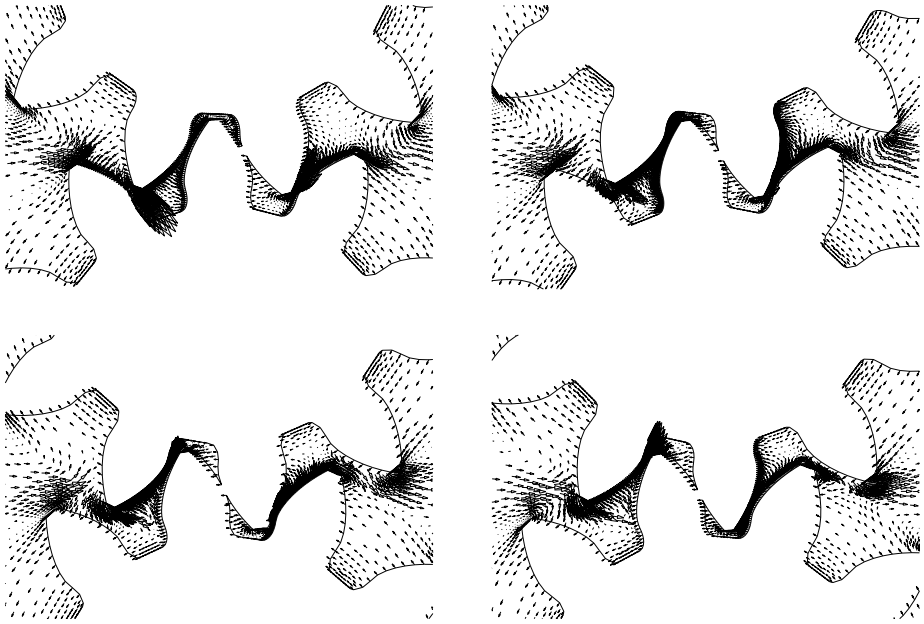

Figure 23: External gear pump. Velocity vectors at different time steps: $3\delta t$, $4\delta t$, $5\delta t$, $6\delta t$.

the gap can be approximated to a planar Couette flow. Let x be the streamwise direction and y be the crosswise direction and assume the flow is fully developed in x. Solving the Navier-Stokes equations in Cartesian coordinates for the velocity $\boldsymbol{u} = [u, v]^t$, we have that

$$\mu \frac{d^2 u}{dx^2} = \frac{dp}{dx}.$$

We solve this equations with boundary conditions $u(y = -H) = U = \omega r_1$ and $u(H) = 0$. The solution is

$$u = \frac{1}{2}\left(\frac{1}{\mu}\frac{dp}{dx}y^2 - \frac{U}{H}y + U - \frac{1}{\mu}\frac{dp}{dx}H^2\right). \tag{7}$$

With positive pressure gradient, we expect the flow to be retarded. In Section 3.5.2 we remarked that almost no pressure was lost nor gained in the cavity formed by two consecutive gears. Therefore we

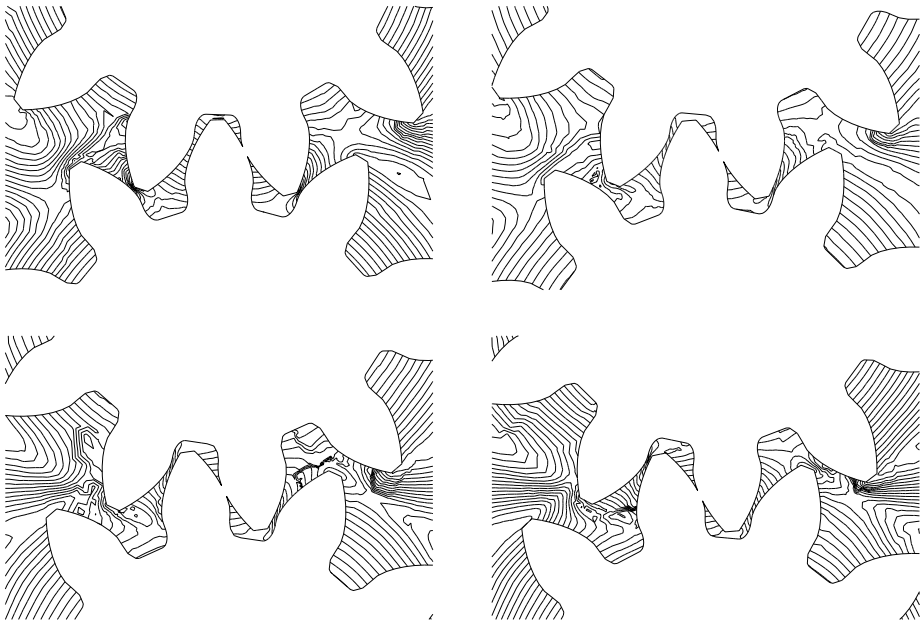

Figure 24: External gear pump. Streamlines at different time steps: $3\delta t$, $4\delta t$, $5\delta t$, $6\delta t$.

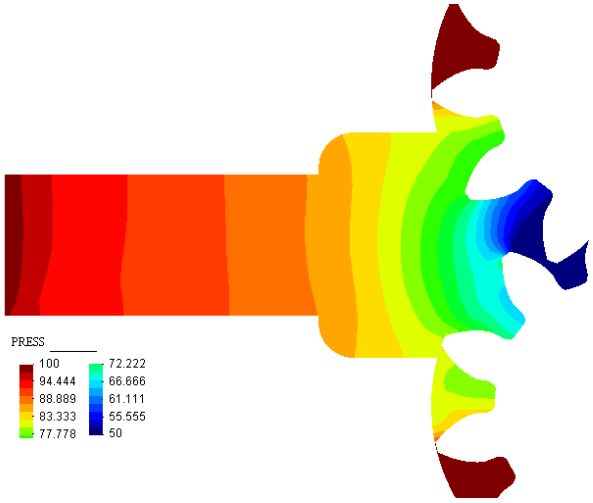

Figure 25: External gear pump. Pressure contours at time step $4\delta t$.

assume that the imposed pressure gradient is entirely distributed over the "contact" zones of the gear with the casing. Let L be the length of these contact zones. We have $L = 1.44\,\text{mm}$. We note that for the geometry considered there are almost seven contact zones. We have therefore

$$\frac{dp}{dx} \approx \frac{p_o - p_a}{7L} = 89.29\ \text{kg/mm}^2\ \text{s}^2. \tag{8}$$

From the solution of the periodic transient Stokes problem we pick up the velocity in the azimuthal direction at the centerline of a gap. More precisely, we consider the gap between the casing and the tooth of the top gear of Figure 19 (Top) (Left) which is about to enter the outport zone. Figure 26 shows the simulation results together with the planar Couette solution given by Equation (7) with the pressure gradient given by Equation (8). For the sake of comparison the solution of the Couette flow without pressure gradient is shown.

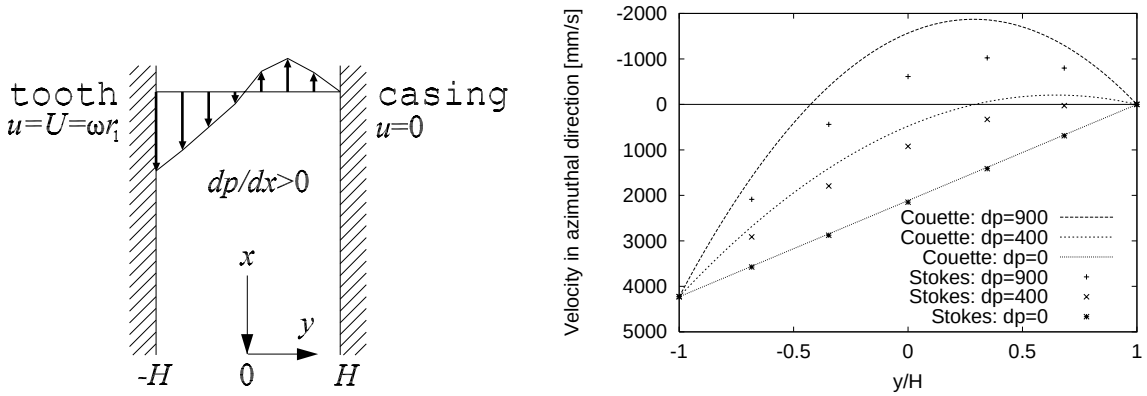

Figure 26: External gear pump. Transient Stokes flow. (Left) Geometry of the gap. (Right) Velocity in gap.

We first note that the flow inside the gap can be well approximated by the solution of the planar Couette flow with adverse pressure gradient. Let us finally note that the local Reynolds number based on $U/2$ and H (by convention for the plane Couette flow) is as low as

$$\mathrm{Re} = \frac{\rho(U/2)H}{\mu} = 4.7.$$

Finally, Figure 27 shows the volume flow rate variation as a function of the pressure gradient imposed between inport and outport. The simulation has been performed on the initial geometry. We compare the simulation with the flow rate we obtain at zero pressure gradient minus the flow due to the Couette profile in the gap (at top and bottom gears); it is given by

$$Q = Q(dp/dx = 0) - \frac{4}{3\mu}\frac{p_o - p_a}{7L}H^3.$$

The results are also compared to that obtained on half of the pump (the suction side) for which no reverse flow exists.

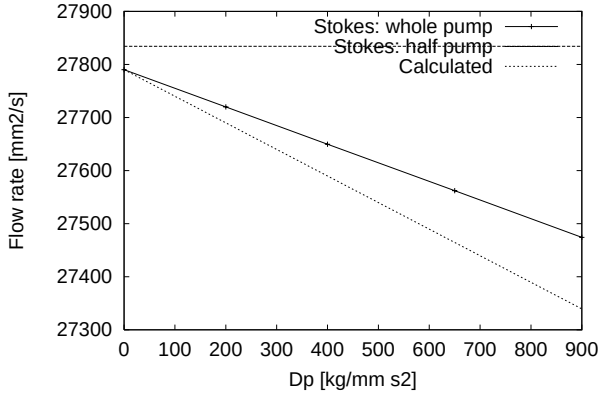

Figure 27: External gear pump. Steady Stokes flow. Flow rate variation as a function of the pressure gradient.

3.5.4 Transient simulation: Navier-Stokes problem

We now go on to the realistic problem by solving the Navier-Stokes equations. When solving the Stokes flow we observed a reverse flow in the gap between the teeth and the casing. We expect this zone to be conflictive as the reverse pressure gradient is highly destabilizing. In addition, the flow in the contact zones of the teeth will not tried to be solved. We thus simplify the goemetry at each time step, as shown for example for time step $3\delta t$ in Figure 28.

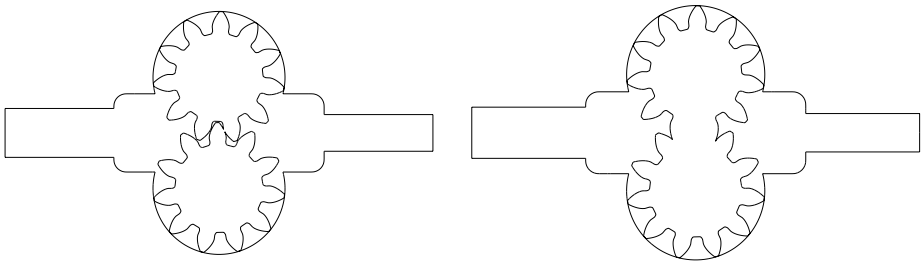

Figure 28: External gear pump. Geometries at time $3\delta t$. (Left) For Stokes. (Right) For Navier-Stokes.

No stationary solution was obtained. However, the changes in the solution from one cycle to the other are small. Figure 29 shows the solution obtained on the initial configuration after some cycles and compares it to the results obtained with a transient Stokes simulation. We observe that including the inertia effects due to the convective term, the recirculation at the outport is greater than that at inport.

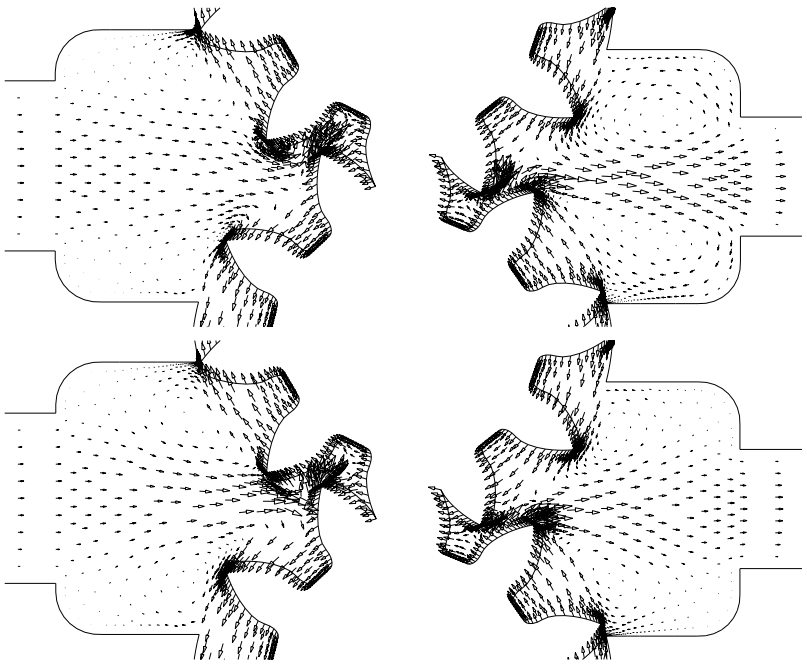

Figure 29: External gear pump. Velocity vectors at inport and outport. (Left) Inport. (Right) Outport. (Top) Transient Navier-Stokes. (Bot.) Transient Stokes.

Figure 30 compares the streamlines obtained with both simulations.

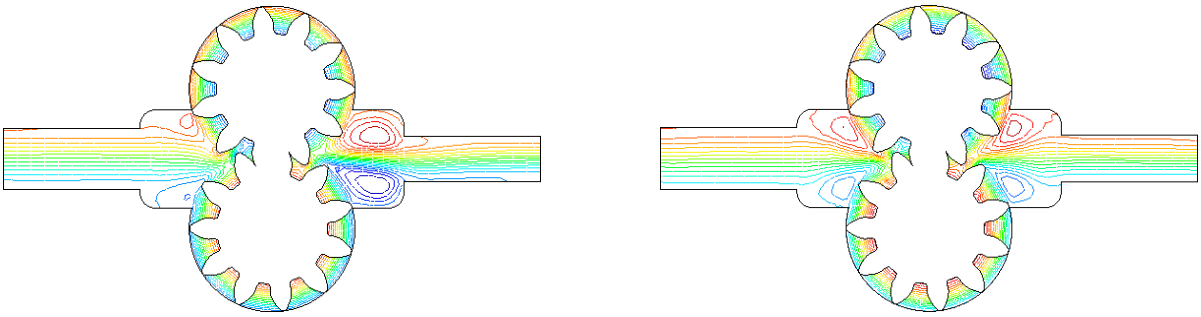

Figure 30: External gear pump. Streamlines. (Left) Transient Navier-Stokes. (Right) Transient Stokes.

3.5.5 3D simulation: Stokes problem

A first simulation of the 3D problem is performed using the following approximation:

- The effects of the gap is neglected so that we only consider the suction side of the pump.
- Flow is considered steady.
- Convection effects are neglected.

The first approximation consists in assuming that the leakage is small and no reverse flow will perturb the incoming one. Therefore we stick the teeth to the body of the pump. The second approximation enables to solve only one configuration of the pump. We take for this simulation the initial position at time 0. Finally, a linear problem is solved as we neglect the convection effects. See for example the 2D comparison between the Stokes and Navier-Stokes flow. Figure 31 shows the results obtained for this flow. With respect to the two-dimensional simulation we observe that the velocity in the inlet pipe is much more rapid, as the same quantity of fluid has to pass through a reduced section.

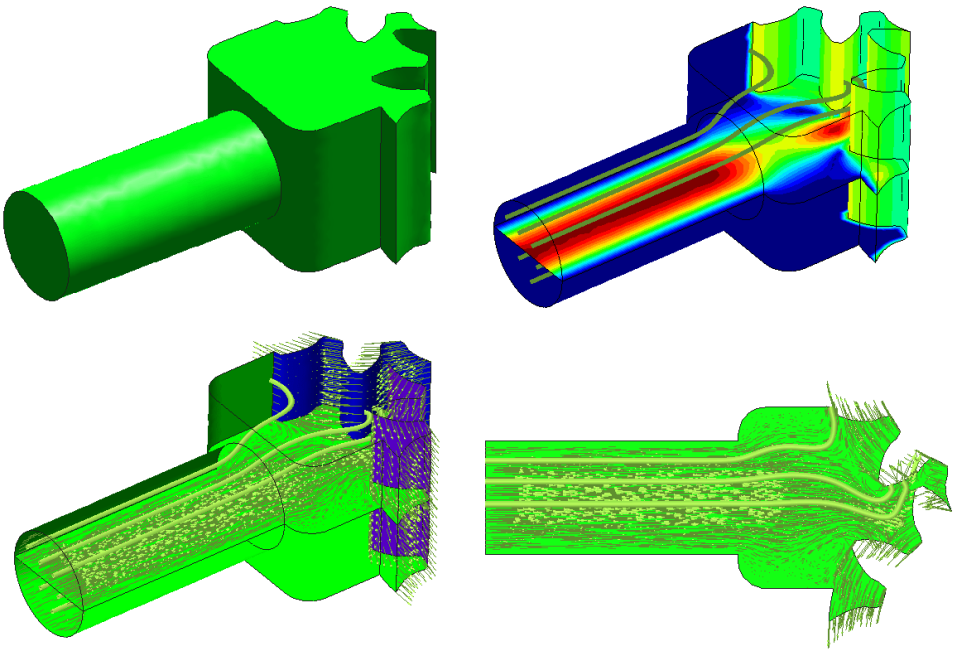

Figure 31: External gear pump. 3D simulation: Stokes problem. (Top) (Left) Geometry. (Top) (Right) Velocity module and streamlines. (Bot.) (Left) Velocity module and vectors. (Bot.) (Right) Velocity module and vectors on symmetry plane.

The transient Stokes equations are now solved at the inport. The numerical strategy is exactly the same than that used for the transient simulation of the two-dimensional sections of this pump. Figure 32 shows the velocity vectors obtained on different section of the initial configuration. We can observe horizontal as well as vertical recirculations beyond the inlet corners. Figure 33 shows the velocity vectors obtained at the four first time steps of a cycle.

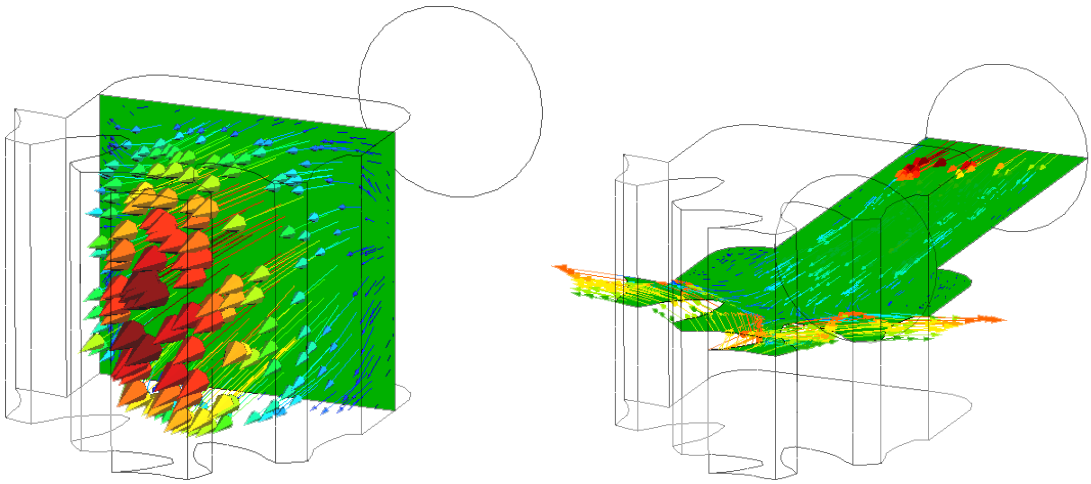

Figure 32: External gear pump. Transient 3D simulation: Stokes problem.

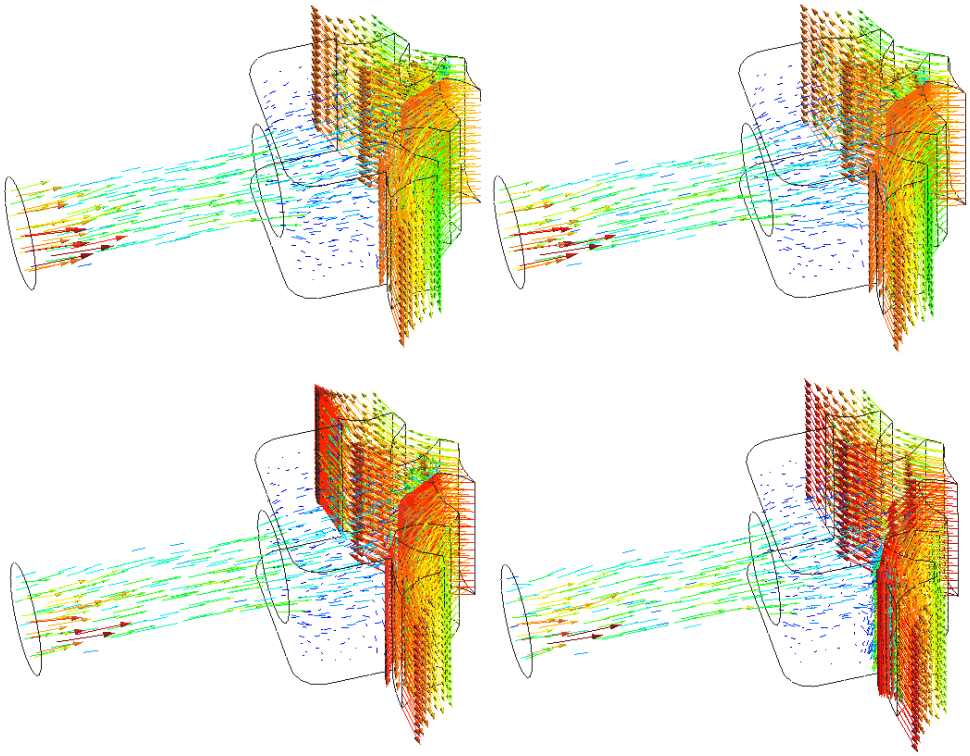

Figure 33: External gear pump. Transient 3D simulation: Stokes problem. Velocity vectors at consecutive time steps.

4 Internal gear pump

4.1 Introduction

The internal gear pump we study is of Gerotor (generated rotor) type. As the external pump described previously, gerotor pumps are of positive displacement. The pump consists of an inner gear and an outer gear, this one having one more tooth. The outer gear is carried around by the inner gear motion, which is driven around by the drive shaft. But the outer gear does not have a fixed center of rotation, so that the casing must contains its displacement.

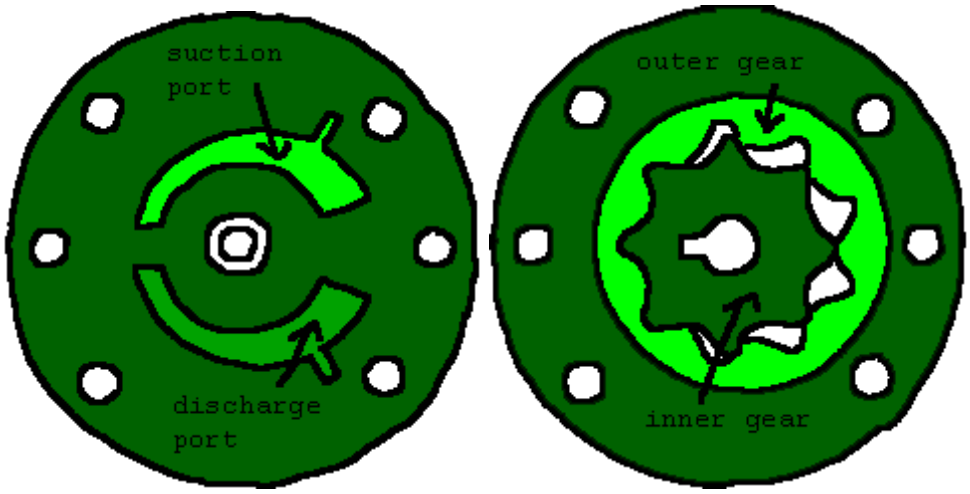

Figure 34: Internal gear pump.

To understand how the pump works, let us consider what is occurring within the cavity limited by two consecutive teeth of the inner gear and the outer gear. Starting from the two teeth defining a minimum volume, we rotate the inner gear until it enters the intake chamber. The cavity volume increases and creates a depressurization to make the fluid fill in the cavity. The oil at the inport comming from a tank being at atmospheric pressure, the pressure at this point falls below the atmospheric pressure. As we rotate further, the cavity volume increases and more and more fluid enters the cavity, until it reaches a maximum volume when it is no longer in contact with the intake chamber. From now the volume decreases and as the cavity is now in contact with the outake, fluid is ejected from the cavity to the outake chamber. As mentioned before, the pressure at the inport is at atmospheric pressure. The pressure at the outport depends on the elements we have in the hydraulic circuit. This means that as for the previous pump studied, the pump delivers flow rate but not pressure. For example, if the oil at intake comes from a tank and the pump delivers it in another tank without any external resistance, then both pressure will be atmospheric. On the contrary, if some resistance is added after the pump (e.g. a pipe), the pressure at the outport will have to increase to overcome the friction.

4.2 Geometry simplification

The geometry of the internal gear pump under study is more complicated than the previous external gear pump. The CAD geometry is sketched in Figure 35.

However, by assuming that there is no gap between the gears and the casing, it can be greatly simplified. In fact, by doing so, we can consider separately the inport and outport. In Figure 35, the inport appears shaded.

In this study we focus on the suction side of the pump. Only the initial configuration of the pump is considered and the flow is assumed steady. That is we solve the stationary Stokes equations. Figure 36 shows the computational domain as well as a finite element mesh of 17177 tetahedra elements and 4546 nodes.

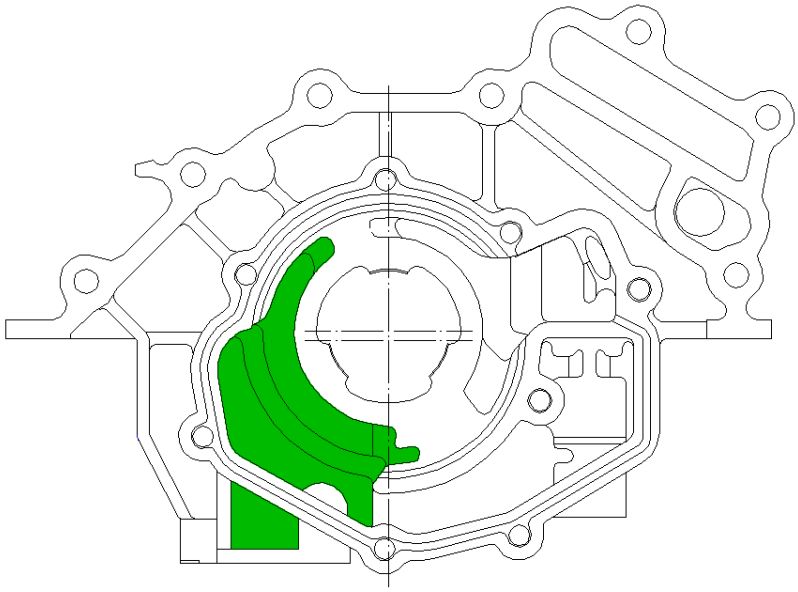

Figure 35: Internal gear pump. CAD geometry of the casing. Suction side is dashed.

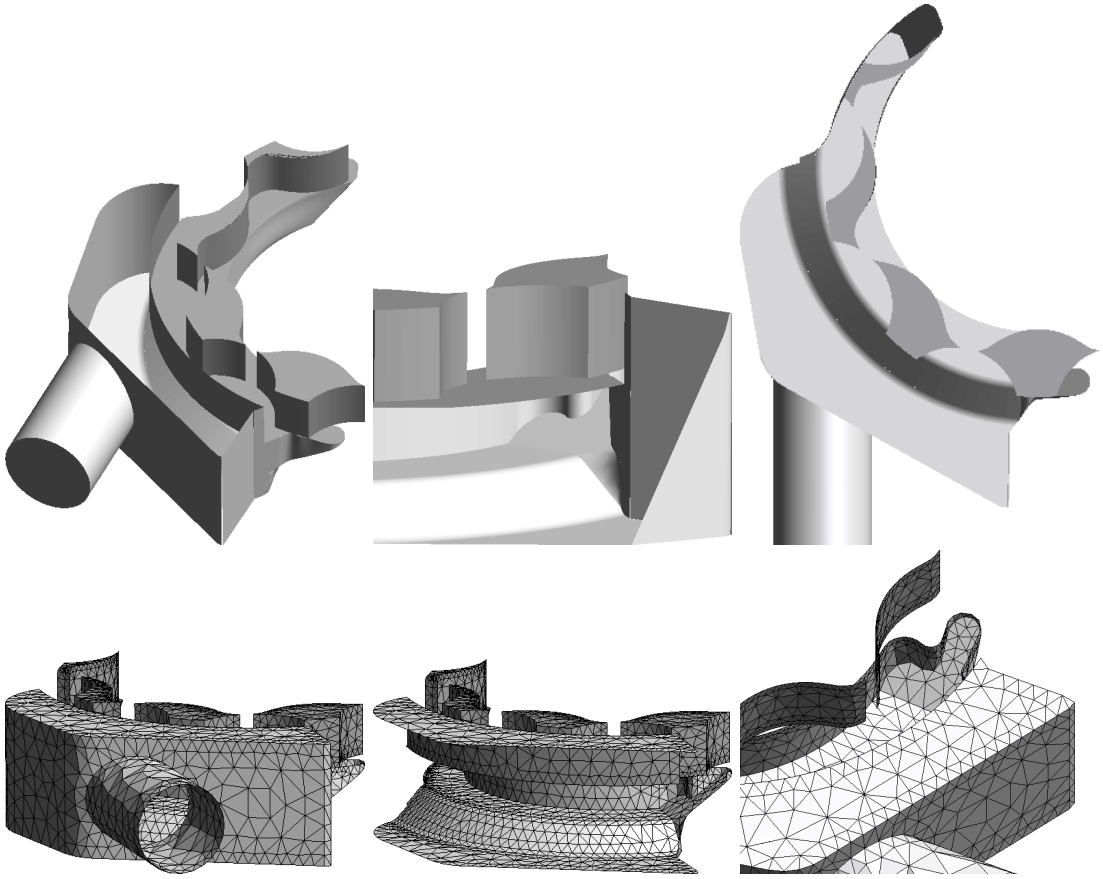

Figure 36: Internal gear pump. (Top) Geometry. (Bot.) Mesh.

4.3 Data of the problem

The oil employed is the same as that employed for the external gear pump. The inner gear is rotating at an angular velocity of 1500 rpm. At the initial configuration, the outer gear is rotating at the same

velocity but its rotation center is located 2.85 mm away from the inner gear rotation center.

4.4 Results

Figure 37 shows some streamlines together with the velocity vectors. We can observe suction of some flow to the opening cavity as well as some flow towards the closing cavity.

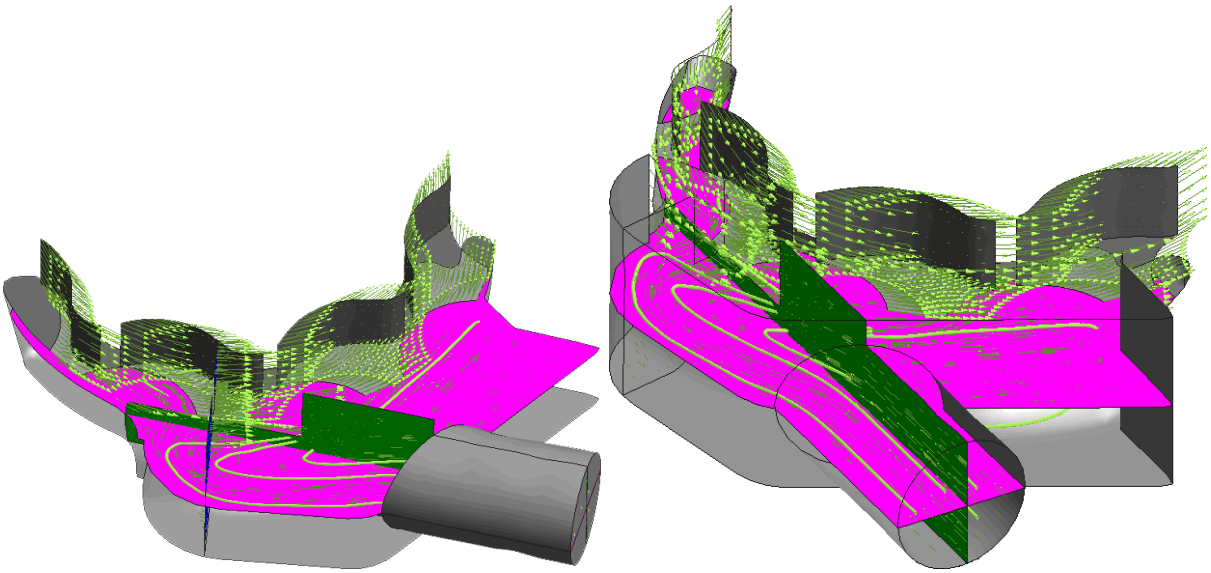

Figure 37: Internal gear pump. Stokes flow. Velocity vectors and streamlines.

References

[1] M.W. Volk. *Pump Characteristics and Applications*. Maral Dekker, Inc., 1996.

[2] G.K. Batchelor. *An Introduction to Fluid Dynamics*. Cambridge University Press, 1970.

[3] R. Codina and O. Soto. Finite element implementation of two-equation and algebraic stress turbulence models for steady incompressible flows. *Int. J. Num. Meth. Fluids*, 30:309–333, 1999.

[4] F. Brezzi and M. Fortin. *Mixed and Hybrid Finite Element Methods*. Springer-Verlag, 1991.

[5] T. J.R. Hughes. Multiscale phenomena: Green's functions, the Dirichlet-to-Neumann formulation, subgrid scale models, bubbles and the origins of stabilized methods. *Comp. Meth. Appl. Mech. Eng.*, 127:387–401, 1995.

[6] R. Codina. A stabilized finite element method for generalized stationary incompressible flows. *Comp. Meth. Appl. Mech. Eng.*, 190, 2001.

[7] R. Codina. On stabilized finite element methods for linear systems of convection-diffusion-reaction equations. *Comp. Meth. Appl. Mech. Eng.*, 188:61–82, 2000.

[8] M. Volk. *Pump Characteristics and Applications*. Marcel Dekker, Inc., 1996.

[9] G. Houzeaux and R. Codina. An iteration-by-subdomain overlapping Dirichlet/Robin domain decomposition method for advection-diffusion problems. *J. Comput. Appl. Math.*, 2001. Submitted.